Research Square

Preprints are preliminary reports that have not undergone peer review.
They should not be considered conclusive, used to inform clinical practice,
or referenced by the media as validated information.

Molecular substitution controls film connectivity and charge transport in pyrene-based organic field-effect transistors

Ziya DAĞALAN
Ataturk University
Fatma BAYRAKÇEKEN NİŞANCI
Ataturk University
Hasan Feyzi BUDAK
Ataturk University
Betül GÜZELDİR
bguzeldir@atauni.edu.tr

Ataturk University

Research Article

Keywords: Pyrene-based semiconductors, Organic field-effect transistors, Substituent engineering, Hole reorganization energy, Film organization, Charge transport

Posted Date: October 20th, 2026

DOI: https://doi.org/10.21203/rs.3.rs-11426639/v1

License: This work is licensed under a Creative Commons Attribution 4.0 International License.
Read Full License

Additional Declarations: No competing interests reported.

Molecular substitution controls film connectivity and charge transport in pyrene-based organic field-effect transistors

Ziya DAĞALAN[a], Fatma BAYRAKÇEKEN NİŞANCI[a], Hasan Feyzi BUDAK[b] and Betül GÜZELDİR[c*]

[a]Department of Chemistry, Faculty of Science, Ataturk University, 25240, Erzurum, Turkey

[b]Eastern Anatolia High Technology Application and Research Center, Ataturk University, 25240, Erzurum, Turkey

[c*]Department of Physics, Faculty of Science, Ataturk University, 25240, Erzurum, Turkey

Abstract

Molecular substitution changes both the intrinsic energetics and solid-state organization of organic semiconductors, yet these effects need not produce the same transistor-performance trends. Here, four pyrene derivatives (Py-1–Py-4) are compared in a common top-gate/bottom-contact organic field-effect transistor architecture to identify how molecular energetics, film connectivity, and device resistance jointly influence hole transport. Density functional theory reveals that Py-3 has the lowest adiabatic ionization potential (6.447 eV), whereas Py-2 has the lowest internal hole reorganization energy (0.178 eV), demonstrating that the molecular relaxation-energy ranking does not predict the mobility ranking. X-ray diffraction and electron/atomic-force microscopy show substituent-dependent structural organization, including interconnected fibrillar domains in Py-3 and heterogeneous aggregation in Py-4. Py-3 achieves the highest field-effect mobility (5.4×10^{-1} cm^2 V^{-1} s^{-1}), an on/off ratio of 8.0×10^4, a subthreshold swing of 1.6 V dec^{-1}, and a threshold-voltage hysteresis of 1.1 V. Channel-length-dependent analysis further identifies the lowest contact and sheet resistances for Py-3, while measurements of three devices per derivative support the reproducibility of the performance hierarchy. The results indicate that effective long-range transport depends on connected film morphology and device interfaces as well as favorable molecular energetics.

Keywords: Pyrene-based semiconductors; Organic field-effect transistors; Substituent engineering; Hole reorganization energy; Film organization; Charge transport

Corresponding author: bguzeldir@atauni.edu.tr (Betül GÜZELDİR)

1. Introduction

Polycyclic aromatic hydrocarbons (PAHs) have attracted considerable attention owing to their unique optoelectronic characteristics, rigid π-conjugated frameworks, and tunable intermolecular electronic interactions. In particular, organic field-effect transistors (OFETs), organic photovoltaics (OPVs), and organic light-emitting diodes (OLEDs) have attracted enormous scientific and technological interest as potential alternatives to conventional inorganic electronics.[1–4] The electrical performance of such organic electronic systems is strongly governed by intermolecular electronic coupling, molecular packing behavior, and nanoscale structural organization within the semiconducting layer.[5–7] Consequently, the rational molecular engineering of π-conjugated semiconductors has become a critical research direction for improving charge transport efficiency and device stability in organic electronics [8].

Among various conjugated aromatic systems, pyrene-based semiconductors have attracted particular attention due to their rigid fused aromatic framework, strong fluorescence, high thermal stability, and favorable intermolecular π–π interactions.[9–11] The extended π-conjugated structure of pyrene facilitates intermolecular orbital overlap and electronic delocalization, both of which are highly advantageous for carrier transport in OFET architectures.[12,13] Furthermore, pyrene derivatives exhibit excellent synthetic tunability, allowing systematic modification of frontier molecular orbital energies, aggregation behavior, optical transitions, and molecular self-assembly characteristics through substituent engineering.[14–16] Such structural flexibility makes pyrene-based systems highly attractive candidates for high-performance organic semiconductor applications.

Nevertheless, despite the intrinsically favorable electronic properties of pyrene cores, the charge-transport performance of pyrene semiconductors remains highly sensitive to substituent-dependent intermolecular organization and film morphology.[17,18] Small variations in molecular architecture can significantly alter molecular planarity, aggregation tendency, intermolecular packing density, and nanoscale surface texture, thereby directly affecting charge-percolation pathways and carrier mobility within organic thin films.[6,19,20] In conjugated organic semiconductors, enhanced directional π–π stacking generally promotes intermolecular charge delocalization and facilitates lateral carrier transport, whereas excessive aggregation and structural disorder may introduce localized trap states and transport nonuniformity.[6,12,22] Therefore, understanding the relationship between molecular structure, nanoscale morphology, intermolecular electronic interaction, and optoelectronic response is critically important for the development of efficient OFET materials.

Recent studies have demonstrated that substituent-controlled intermolecular organization can strongly influence optical absorption behavior, excited-state relaxation dynamics, and carrier transport mechanisms in conjugated aromatic systems.[23–25] In particular, donor/acceptor-type molecular engineering approaches involving methoxy and nitro functional groups have been shown to effectively modulate intermolecular electronic coupling and frontier orbital distribution within π-conjugated frameworks.[2,26] Such substituent-induced electronic modulation can substantially affect molecular aggregation characteristics and thin-film morphology, which are key parameters governing OFET transport behavior.[1,5,6]

Although a growing number of pyrene derivatives have been explored as organic semiconductors, including recent molecular-engineering strategies based on substitution-site control and heteroatom incorporation, the resulting transistor performance remains strongly dependent on molecular architecture, solid-state organization, and device configuration [22–24,56]. Recent studies further demonstrate that controlled modification of the pyrene framework can produce pronounced changes in molecular conformation, packing motifs, film morphology, and carrier transport [35,56]. Nevertheless, comparatively few studies have examined how systematic substituent variation within a common pyrene molecular platform propagates simultaneously through optical response, nanoscale film organization, interfacial trapping, contact and channel resistance, and statistically reproducible OFET characteristics under an identical device architecture. Establishing these interconnected relationships is particularly important for distinguishing beneficial molecular organization from aggregation that does not translate into efficient long-range field-effect transport.

In this work, a series of structurally engineered pyrene-based semiconductor derivatives (Py-1–Py-4) were successfully synthesized via Suzuki cross-coupling reactions using pyren-1-ylboronic acid and various aryl bromide precursors. Methoxy- and nitro-containing substituent architectures were systematically incorporated into the pyrene framework in order to modulate intermolecular electronic coupling, aggregation characteristics, and conjugation behavior. The synthesized compounds were comprehensively characterized using FTIR, UV–Vis absorbance spectroscopy, photoluminescence (PL), X-ray diffraction (XRD), scanning electron microscopy (SEM), atomic force microscopy (AFM), NMR, and ESI-QTOF analyses. The combined optical, diffraction, and morphological investigations revealed pronounced substituent-dependent differences in solid-state organization, excited-state electronic interactions, and nanoscale surface morphology. Complementary DFT calculations were employed to evaluate substituent-dependent frontier-orbital characteristics, adiabatic ionization energetics, and internal hole reorganization energies, thereby providing a

molecular-level energetic framework for comparison with the experimentally observed transport behavior. Importantly, these intrinsic molecular descriptors were interpreted together with film morphology and device characteristics to distinguish favorable molecular energetics from the solid-state organization required for efficient long-range field-effect transport. Furthermore, the synthesized pyrene derivatives were evaluated as active semiconducting layers for OFET applications in order to establish a comprehensive structure–energetics–morphology–interface–transport relationship for pyrene-based organic semiconductors. The results demonstrate that molecular substituent engineering provides an effective strategy for tailoring intermolecular π–π interactions and charge-transport characteristics in conjugated pyrene semiconductor systems.

2. Experimental Section

2.1. Materials

Pyren-1-ylboronic acid, palladium(II) acetate ($Pd(OAc)_2$), sodium carbonate (Na_2CO_3), tetrabutylammonium bromide (TBABr), ethyl acetate, petroleum ether, and all other commercially available solvents and reagents were purchased from standard chemical suppliers and used without further purification unless otherwise specified. The aryl bromide precursors used in the Suzuki cross-coupling reactions were synthesized according to previously reported procedures, while one precursor was obtained commercially.

2.2. Synthesis of Pyrene-Based Semiconductor Derivatives

The pyrene-based semiconductor derivatives (Py-1–Py-4) were synthesized through Suzuki cross-coupling reactions between pyren-1-ylboronic acid and the corresponding aryl bromide precursor molecules. In a typical synthesis procedure, aryl bromide precursor (5.15 mmol), pyren-1-ylboronic acid (5.15 mmol), Na_2CO_3 (15.45 mmol), $Pd(OAc)_2$ catalyst (0.00206 mmol), and TBABr (5.15 mmol) were introduced into a 25 mL round-bottom flask containing 10 mL deionized water together with a magnetic stir bar. The reaction mixture was gradually heated from room temperature to 150 °C and maintained at this temperature for 30 min under continuous stirring.

After completion of the reaction, the mixture was cooled to room temperature and transferred into a separatory funnel. The reaction products were extracted using ethyl acetate and water (30 mL each). The organic phases were combined and dried over anhydrous Na_2SO_4, then concentrated under reduced pressure. The crude products were purified by column chromatography on silica gel using an

ethyl acetate/petroleum ether eluent system, yielding yellow pyrene derivatives with isolated yields ranging from 85% to 92%.

The synthesized compounds were structurally characterized using 1H NMR, 13C NMR, and ESI-QTOF mass spectrometry. Detailed molecular characterization data, together with complete NMR and ESI-QTOF spectra, are provided in the Supporting Information section.

2.3. Thin-Film Preparation

Thin films of the synthesized pyrene-based semiconductor derivatives (Py-1–Py-4) were prepared on ITO-coated glass substrates by spin coating. Prior to film deposition, the substrates were sequentially cleaned by ultrasonication in acetone, isopropanol, and deionized water and subsequently dried under a nitrogen atmosphere. The synthesized pyrene derivatives were dissolved in chloroform at a concentration of 10 mg mL^{-1} to prepare the semiconductor solutions. The resulting solutions were deposited onto the cleaned ITO-coated glass substrates by spin coating at 1500 rpm for 60 s. Following deposition, the semiconductor films were thermally annealed at 100 °C for 5 min to remove residual solvent and obtain uniform semiconductor layers suitable for subsequent characterization and device fabrication.

2.4. OFET Fabrication

OFET devices were fabricated on pre-patterned indium tin oxide (ITO) substrates, which served as source and drain electrodes. Prior to device fabrication, the patterned ITO substrates were sequentially cleaned with acetone, isopropanol, and deionized water under ultrasonication, then dried under a nitrogen atmosphere.

The synthesized pyrene-based semiconductor derivatives (Py-1–Py-4) were deposited onto the patterned ITO source/drain substrates using the same spin-coating and thermal-annealing conditions described in Section 2.3, thereby forming the active semiconductor channel layers. Following semiconductor deposition, poly (isobutyl methacrylate) (PiBMA) was employed as the dielectric layer owing to its excellent insulating behavior, smooth surface morphology, and compatibility with organic semiconductor systems. The PiBMA/toluene solution (30 mg mL^{-1}) was prepared under continuous magnetic stirring and deposited onto the semiconductor-coated substrates by spin coating at 1500 rpm. After the coating process, the PiBMA dielectric films were thermally dried at 110 °C for 10 min in order to remove residual solvent and improve dielectric film uniformity.

Finally, Al gate electrodes were thermally evaporated onto the PiBMA/semiconductor/ITO structure, completing the OFET device architecture. During metal deposition, the evaporation rate was

maintained at 1 Å s^{-1} and the Al gate thickness was fixed at 100 nm. The resulting PiBMA dielectric thickness was approximately 100 nm.

2.5. Characterization and Electrical Measurements

Fourier-transform infrared (FTIR) spectra were recorded within the 4000–400 cm^{-1} spectral range in order to investigate the vibrational characteristics of the synthesized pyrene derivatives. UV–Vis absorbance measurements were performed over the 300–700 nm wavelength range to evaluate the optical transition behavior and conjugation characteristics of the semiconductor films. Photoluminescence (PL) spectra were measured under 325 nm excitation in order to investigate excited-state recombination and intermolecular electronic interaction behavior.

X-ray diffraction (XRD) patterns were recorded using a Rigaku MiniFlex goniometer equipped with Cu Kα radiation (λ = 1.5406 Å). The diffraction profiles were evaluated over the common 2θ range of 5–80° for comparison of the Py-1–Py-4 derivatives. Interplanar spacings were calculated using Bragg's law, $d = \lambda/(2 \sin \theta)$, and apparent coherent-domain sizes were estimated using the Scherrer relation, $D = K\lambda/(\beta \cos \theta)$, with K = 0.9 and β expressed as the full width at half maximum (FWHM) in radians.

The surface morphologies of the synthesized pyrene films were investigated using scanning electron microscopy (SEM) and atomic force microscopy (AFM). SEM analyses were employed to evaluate the microstructural organization and aggregation characteristics of the semiconductor surfaces, whereas AFM measurements provided detailed nanoscale topographical information regarding surface organization, domain morphology, and roughness evolution.

The molecular structures of the synthesized compounds were confirmed using 1H NMR, 13C NMR, and electrospray ionization quadrupole time-of-flight mass spectrometry (ESI-QTOF).

The electrical characteristics of the fabricated OFET devices were measured at room temperature using a Keithley 2634B dual-source meter/voltage source under ambient conditions. Transfer and output characteristics were systematically recorded in order to evaluate the charge-transport behavior of the pyrene-based semiconductor layers. The electrical parameters obtained, including field-effect mobility, threshold voltage, subthreshold swing, and current on/off ratio, were extracted from the transfer characteristics and compared with the substituent-dependent optical and morphological properties of the synthesized semiconductor systems.

The field-effect mobility (μ_{FE}) was extracted in the saturation regime from the linear region of the $\sqrt{I_D}$–V_{GS} characteristics according to

$$\mu_{FE} = \frac{2L}{WC_{ox}}\left(\frac{d\sqrt{I_D}}{dV_G}\right)^2 \quad (1)$$

where W and L represent the channel width and channel length, respectively, and Cox is the gate-dielectric capacitance per unit area. For the representative OFET mobility calculations, the reported effective channel width was 1000 μm and channel length 50 μm (W/L = 20). The same nominal width was used for the separate TLM devices, whose channel lengths were varied. The PiBMA gate dielectric had a thickness of approximately 100 nm, and Cox was estimated according to

$$C_{ox} = \frac{\varepsilon_0 \varepsilon_r}{t} \quad (2)$$

The gate-dielectric capacitance per unit area was estimated using $C_{ox} = \varepsilon_0\varepsilon_r/t$, with an assumed PiBMA relative permittivity of $\varepsilon_r = 3.9$ and a nominal dielectric thickness of 100 nm. This gives $C_{ox} \approx 34.5$ nF cm^{-2}. Because capacitance was not independently measured, the reported mobilities depend on this estimate.

We recorded transfer characteristics at a constant drain voltage of $V_{DS} = -30$ V, and measured output characteristics by sweeping the drain voltage in the negative-bias regime under systematically varied negative gate biases.

2.6. Computational Methods

Density functional theory (DFT) calculations were performed using the PySCF quantum-chemistry framework [57] to investigate the substituent-dependent molecular electronic structure and intrinsic hole-transport energetics of Py-1–Py-4. The neutral molecules were geometry-optimized at the B3LYP/6-31G(d,p) level using a restricted Kohn–Sham (RKS) formalism. The corresponding radical cations were independently optimized at the same level of theory using unrestricted Kohn–Sham (UKS) calculations with a total charge of +1 and a doublet spin state. Tight self-consistent-field convergence criteria were employed for the final electronic-structure calculations. Frontier orbital energies were obtained from the optimized neutral-state calculations.

The adiabatic ionization potential (IP_{ad}) was determined from the total-energy difference between the independently optimized radical-cation and neutral states according to Eq. (3):

$$IP_{ad} = E^{+}(Q_{+}) - E^{0}(Q_{0}) \quad (3)$$

where Q_0 and Q_+ denote the optimized geometries of the neutral and radical-cation states, respectively. This ΔSCF treatment explicitly accounts for molecular relaxation following oxidation rather than estimating the ionization energetics solely from the neutral-state HOMO energy.

The internal hole reorganization energy (λ_h) was evaluated using the four-point approach [12], according to Eq. (4):

$$\lambda_h = [E^{+}(Q_0) - E^{+}(Q_{+})] + [E^{0}(Q_{+}) - E^{0}(Q_0)] \quad (4)$$

where $E^{+}(Q_0)$ is the single-point energy of the radical cation evaluated at the optimized neutral geometry and $E^{0}(Q_{+})$ is the single-point energy of the neutral molecule evaluated at the optimized radical-cation geometry. The four energy terms were evaluated consistently at the B3LYP/6-31G(d,p) level. The resulting λ_h values therefore represent the intramolecular structural relaxation contribution associated with hole formation; environmental polarization and intermolecular electronic coupling are not included in this molecular-level descriptor.

The calculated quantities are used here to identify substituent-dependent intrinsic molecular trends and are interpreted together with, rather than as substitutes for, the experimentally determined electrochemical, morphological, interfacial, and transistor characteristics. Complete optimized-state and cross-geometry energies, spin-state diagnostics, and additional computational data are provided in the Supporting Information.

3. Results and Discussion

3.1. Molecular Design and Synthetic Strategy

Figure 1a presents the optical photographs of the synthesized pyrene-based semiconductor derivatives in both solution and powder forms, while Figure 1 b–e show the corresponding thin films deposited on ITO substrates. Distinct color variations and interference features observed among the films indicate successful thin-film formation together with substituent-dependent differences in film homogeneity and molecular organization.

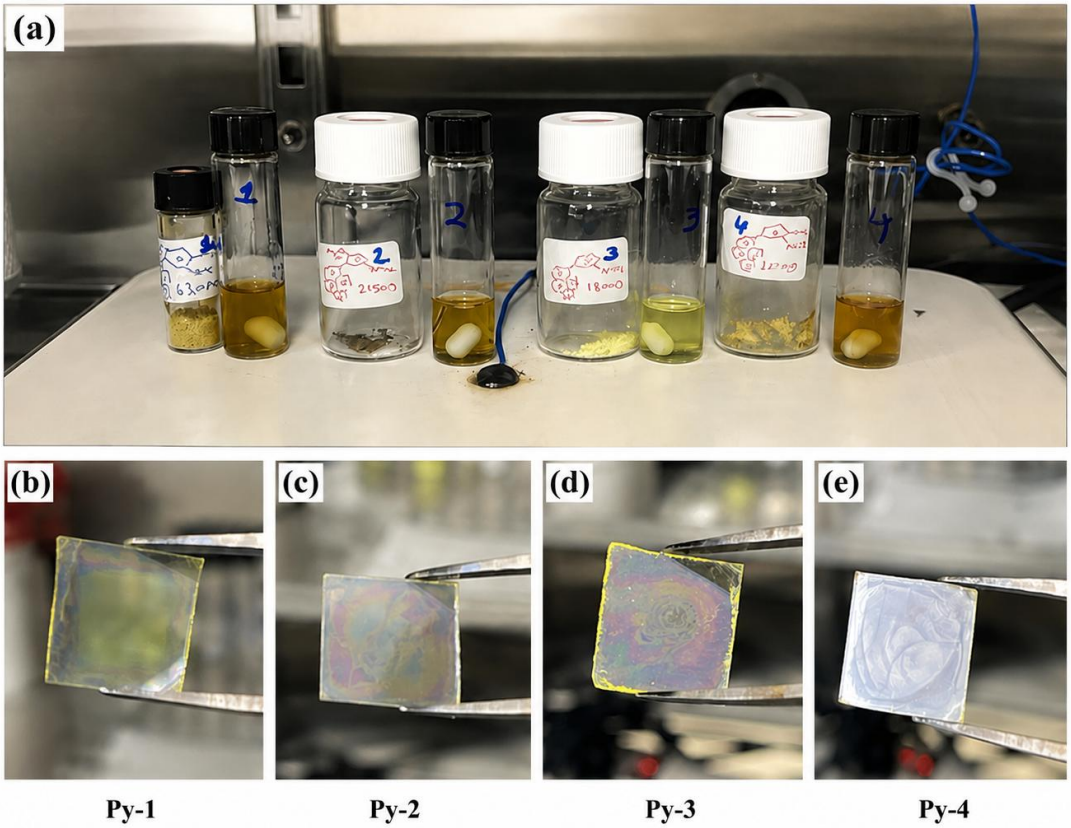
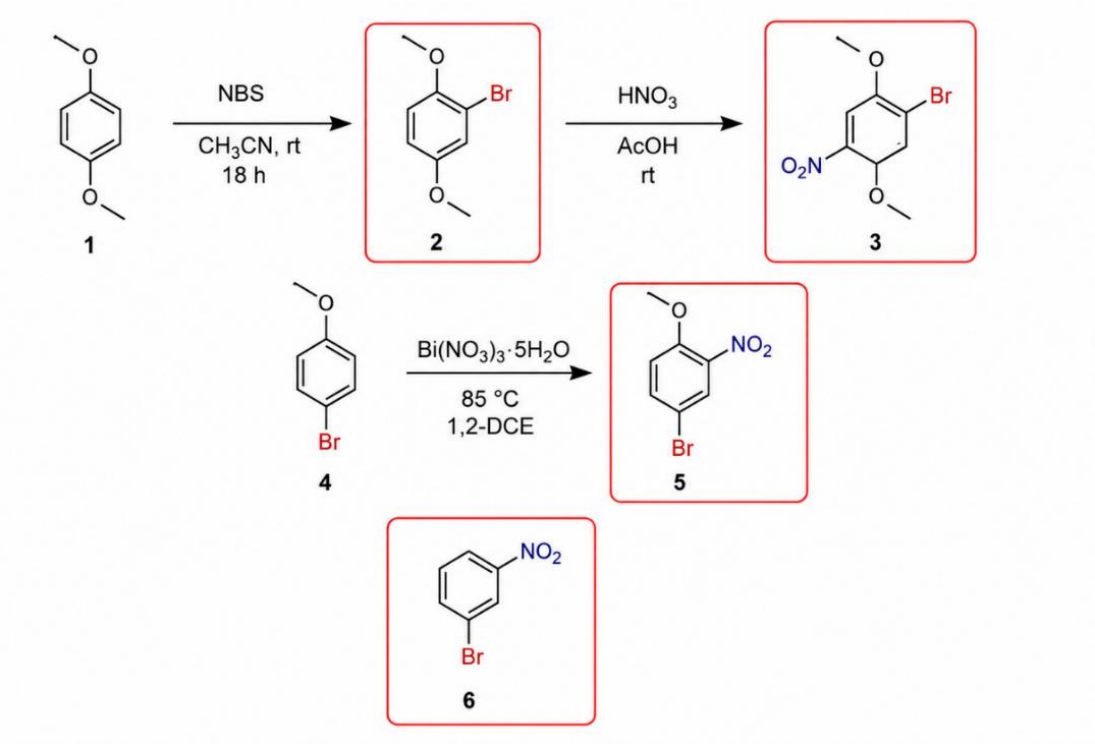
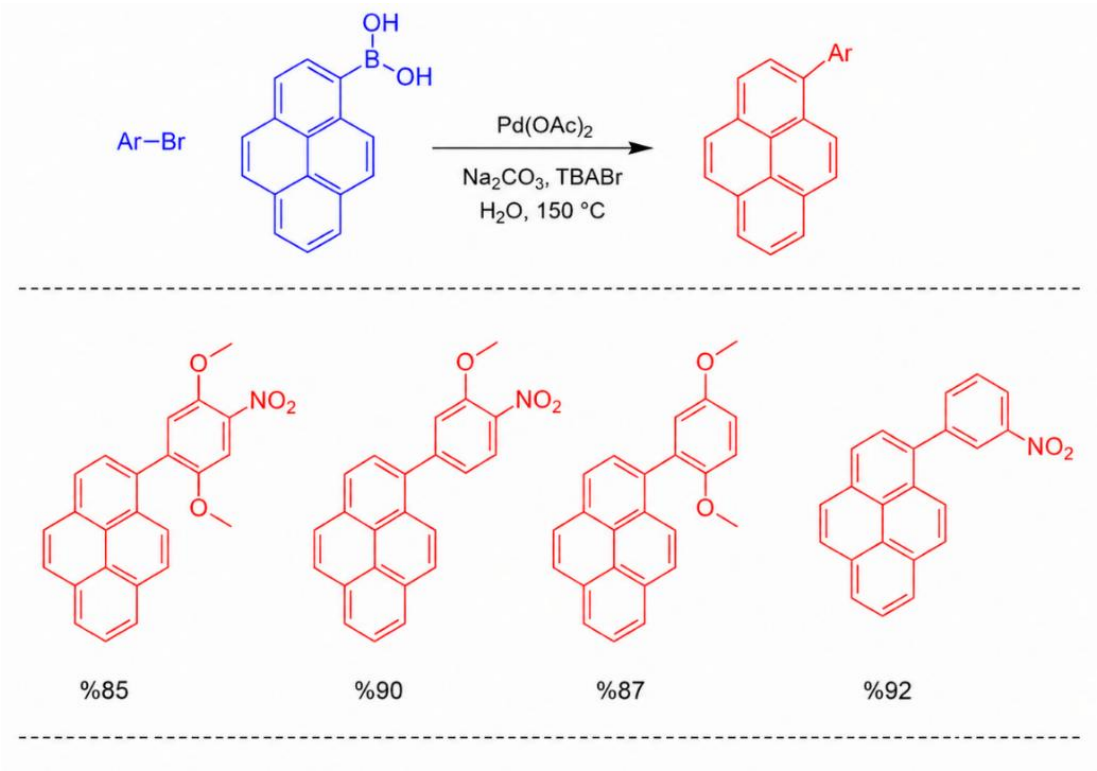


Figure 1. (a) Photographs of the synthesized pyrene-based semiconductor derivatives in solution and powder form. (b–e) Enlarged optical photographs of the corresponding thin films deposited on ITO-coated glass substrates: (b) Py-1, (c) Py-2, (d) Py-3, and (e) Py-4. Distinct interference colors and surface appearances observed in the deposited films indicate successful thin-film formation and suggest notable differences in film-thickness uniformity, molecular organization, and surface homogeneity depending on the molecular substituent structure.

Scheme 1 illustrates the synthetic pathway employed for the preparation of the aryl bromide precursor compounds used in the fabrication of the pyrene-based semiconductor derivatives. Bromination and nitration reactions were used to obtain the corresponding monobromide intermediates bearing different electron-donating and electron-withdrawing substituents. Subsequently, Suzuki cross-coupling reactions between the prepared aryl bromide precursors and pyren-1-ylboronic acid yielded the target pyrene derivatives (Py-1–Py-4), as schematically summarized in Scheme 2.



Scheme 1. Synthetic pathway for the preparation of aryl bromide precursor compounds used in the fabrication of pyrene-based semiconductor derivatives. Bromination and nitration reactions were employed to synthesize the intermediate monobromide structures via controlled substitution under varying reaction conditions. The resulting precursor molecules bearing methoxy and nitro functional groups were subsequently used in Suzuki cross-coupling reactions to construct extended pyrene-conjugated semiconductor architectures.



Scheme 2. Schematic illustration of the Suzuki cross-coupling synthesis route employed for the preparation of pyrene-based semiconductor derivatives. Pyren-1-ylboronic acid was reacted with different aryl bromide precursors in the presence of $Pd(OAc)_2$ catalyst, Na_2CO_3 base, and TBABr additive in aqueous medium at 150 °C, leading to the formation of conjugated pyrene derivatives with high isolated yields ranging from 85% to 92%. The synthesized molecular structures exhibit different substituent architectures designed to modulate intermolecular interaction, conjugation behavior, and optoelectronic properties of the resulting organic semiconductor systems.

The successful formation of the synthesized pyrene derivatives was comprehensively verified using 1H NMR, 13C NMR, and ESI-QTOF analyses. Complete spectral characterization data, molecular geometry representations, frontier-orbital information, and additional electrochemical and computational parameters are presented in the Supporting Information (Figures S1–S9 and Tables S1–S4).

The incorporation of methoxy- and nitro-containing substituent architectures was intentionally designed to modulate intermolecular electronic coupling, aggregation behavior, and molecular packing characteristics within the conjugated pyrene framework. Such substituent engineering is expected to strongly influence optical transitions, nanoscale morphology, and charge-transport pathways in the resulting semiconductor systems.

3.2. FTIR Analysis

The FTIR spectra of the synthesized pyrene-based semiconductor derivatives (Py-1–Py-4) are presented in Figure 2. All samples exhibited characteristic vibrational features associated with π-conjugated aromatic frameworks together with substituent-dependent molecular functionalities, confirming the successful formation of the designed pyrene-based semiconductor architectures [3,9]. The appearance of similar backbone-related vibrational modes across all derivatives additionally indicates that the conjugated pyrene core remained structurally preserved after the Suzuki cross-coupling reactions.

As shown in Figure 2, all derivatives exhibited weak but distinguishable aromatic C–H stretching vibrations centered near ~3045 cm^{-1}, which are characteristic of fused aromatic and pyrene-based conjugated systems.[9,27] In addition, the pronounced absorption bands observed around ~1600 cm^{-1} were attributed to aromatic C=C skeletal stretching vibrations originating from the extended π-conjugated pyrene framework.[3,8] The persistence of these vibrational features across the entire derivative series confirms the successful construction of the aromatic semiconductor backbone.

More importantly, distinct substituent-dependent spectral variations were observed in the fingerprint region (1500–700 cm^{-1}), indicating substantial modulation of the local vibrational environment by molecular architecture. The absorption bands detected between ~1515 and ~1345 cm^{-1} were associated with aromatic skeletal deformation together with C–N and NO_2-related vibrational contributions originating from nitro-containing substituent groups. [28,29] The appearance and evolution of these bands clearly support the successful incorporation of electron-withdrawing nitro functionalities into the conjugated pyrene structures.

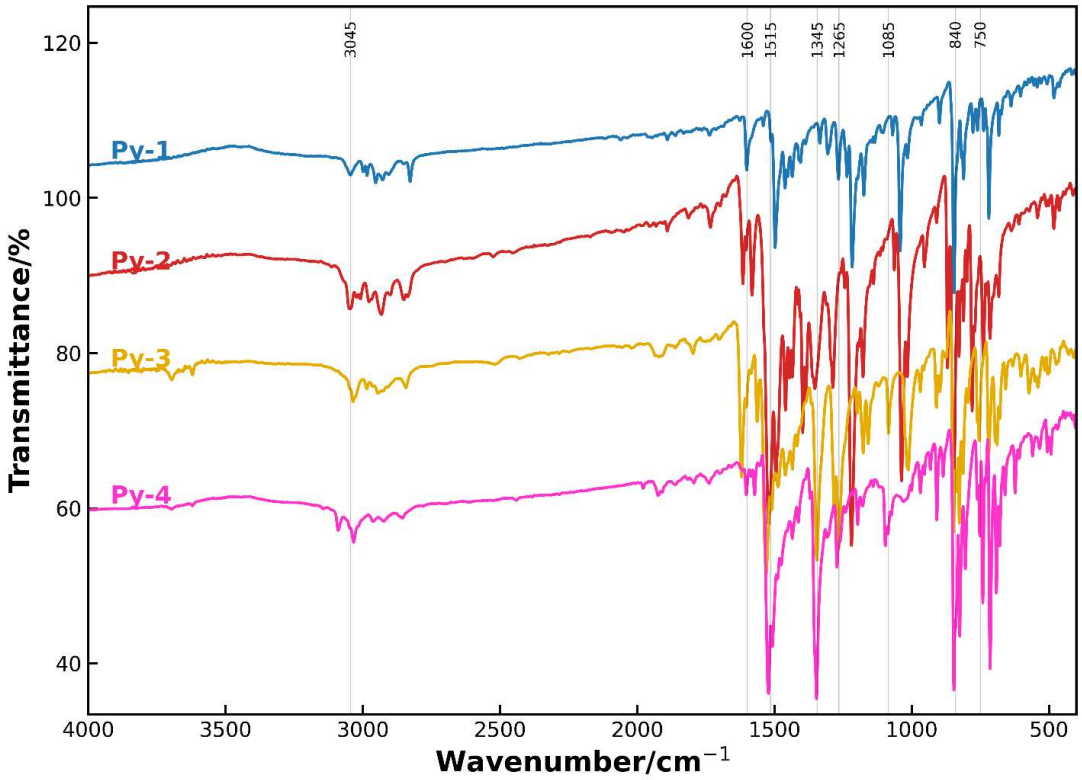


Figure 2. FTIR spectra of the synthesized pyrene-based derivatives (Py-1 to Py-4) recorded in the 4000–400 cm^{-1} region. The spectra exhibit the characteristic vibrational features of π-conjugated aromatic frameworks, including aromatic C–H stretching vibrations observed around ~3045 cm^{-1}, aromatic C=C skeletal stretching modes near ~1600 cm^{-1}, and prominent fingerprint-region bands between 1500–700 cm^{-1} associated with substituent-dependent ring vibrations, C–O/C–N stretching, and aromatic C–H out-of-plane deformation modes. The systematic variations in the fingerprint region confirm the successful structural modification of the pyrene backbone and the formation of distinct substituted pyrene architectures.

Furthermore, the intense absorption bands located between ~1265 and ~1085 cm^{-1} were attributed to Ar–O–C and C–O stretching vibrations, particularly for methoxy-substituted pyrene derivatives. [2,3] Variations in the relative intensity and spectral distribution of these bands indicate that methoxy-containing substituents modify the local vibrational and bonding environments within the conjugated framework. Such substituent-dependent vibrational evolution further supports the successful structural differentiation of the synthesized pyrene derivatives.

Additionally, the absorption bands observed within the ~840–750 cm^{-1} region were assigned to aromatic C–H out-of-plane deformation vibrations, which are highly sensitive to substitution patterns in fused aromatic compounds. [27,30] The subtle spectral shifts and intensity differences detected in

this region further confirm the structural differentiation among Py-1–Py-4 and demonstrate that substituent engineering directly affects the vibrational behavior of the pyrene skeleton.

Overall, the FTIR analyses confirm the successful synthesis of structurally modified pyrene derivatives and reveal clear substituent-dependent vibrational evolution within the conjugated aromatic framework. Such molecular-level structural modulation may subsequently influence intermolecular interactions, electronic delocalization, and charge-transport characteristics in organic semiconductor and OFET applications [2,8].

3.3. UV–Vis Optical Properties

The UV–Vis absorbance spectra of the synthesized pyrene-based semiconductor derivatives (Py-1–Py-4) are presented in Figure 3. All samples exhibited strong absorption features within the near-ultraviolet region, which are primarily associated with π–π* electronic transitions originating from the extended conjugated pyrene framework. [3,9] The observed spectral evolution clearly demonstrates that molecular substituent engineering strongly affects intermolecular electronic interaction, conjugation behavior, and optical transition characteristics within the synthesized semiconductor systems.

Among the investigated derivatives, Py-2 exhibited the highest absorbance intensity, together with a relatively red-shifted absorption maximum near 351 nm. The red-shifted spectral response is consistent with substituent-dependent modification of the electronic environment and may reflect differences in conjugation and intermolecular interactions within the film [2,6]. Because the absolute absorbance intensity can also depend on film thickness and optical density, the higher intensity observed for Py-2 is not considered independently as direct evidence of stronger molecular packing.

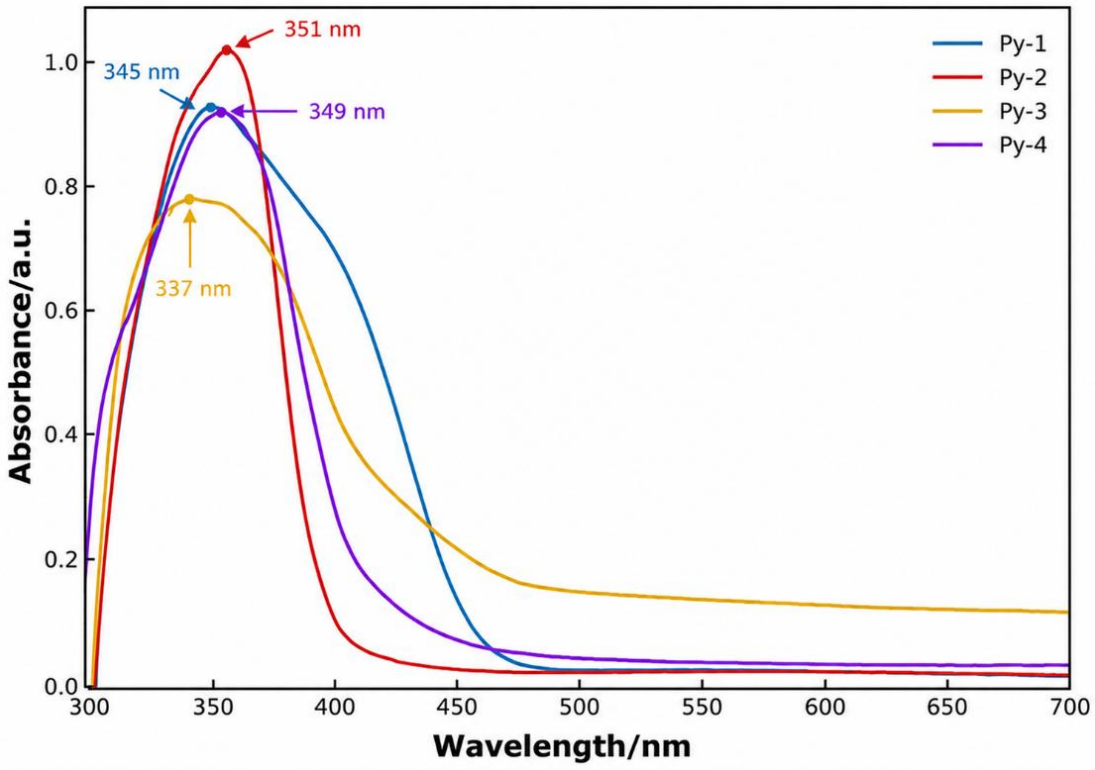


Figure 3. UV–Vis absorbance spectra of the synthesized pyrene-based semiconducting derivatives (Py-1, Py-2, Py-3, and Py-4) recorded in the 300–700 nm wavelength range. All samples exhibit pronounced near-UV absorption features associated with π–π* electronic transitions within the conjugated pyrene framework. Variations in absorption maxima, spectral width, and low-energy absorption tails demonstrate clear substituent-dependent modulation of the optical response. Py-2 and Py-4 exhibit absorption maxima at approximately 351 and 349 nm, respectively, whereas Py-3 shows a comparatively blue-shifted maximum near 337 nm. These spectral differences indicate distinct electronic environments among the four derivatives and are considered together with the complementary PL and morphological analyses when evaluating substituent-dependent film organization.

A similar but slightly less pronounced red-shifted absorption behavior was observed for Py-4, which exhibited an absorption maximum around 349 nm. Its relatively broadened absorption profile is consistent with a more heterogeneous electronic environment and may include contributions from intermolecular interactions within the solid-state film [5]. In conjugated organic semiconductors, spectral broadening and red shifts can accompany changes in intermolecular electronic coupling and aggregation behavior [1,6].

In contrast, Py-3 exhibited a comparatively blue-shifted absorption maximum near 337 nm together with a broad, low-intensity tail extending into the visible region. This distinct spectral response indicates that the ground-state optical environment of Py-3 differs from those of the other derivatives

[3,22]. Importantly, the blue-shifted absorption maximum alone does not imply poorer solid-state organization, because absorption, excited-state relaxation, and mesoscale film morphology probe different aspects of the molecular semiconductor. The optical response of Py-3 is therefore interpreted together with its PL, SEM, AFM, and electrical characteristics rather than being assigned directly to a specific packing motif.

The intermediate spectral position and moderate broadening of Py-1 indicate an optical environment distinct from those of Py-2–Py-4, further supporting substituent-dependent modulation of the electronic response [2,5].

Overall, the UV–Vis analyses demonstrate that molecular substitution significantly influences the optical transition behavior of the pyrene-based semiconductor series. The observed spectral differences are consistent with substituent-dependent changes in the electronic environment and are considered alongside complementary PL and morphological analyses in evaluating film organization [1,6].

The gradual spectral broadening observed, particularly for Py-3 and Py-4, indicates a broader distribution of optical transition environments, which may arise from multiple contributions, including intermolecular interactions and structural heterogeneity [22].

The substituent-dependent optical evolution observed in the UV–Vis spectra is highly consistent with the SEM and AFM analyses, which revealed clear differences in molecular aggregation behavior and nanoscale surface organization among the synthesized derivatives.

3.4. Photoluminescence Characteristics

The PL spectra of the synthesized pyrene-based semiconductor derivatives (Py-1–Py-4) are presented in Figure 4. All samples exhibited broad visible-region emission bands originating from radiative recombination processes within the conjugated pyrene framework. [3,9] The observed emission characteristics strongly depended on the molecular substituent structure, indicating substantial differences in intermolecular electronic interaction, aggregation behavior, and excited-state relaxation dynamics among the synthesized semiconductor systems.

Among the investigated derivatives, Py-2 exhibited a pronounced blue-shifted emission centered near ~464 nm. Such relatively short-wavelength emission behavior generally indicates reduced intermolecular aggregation and weaker excimer-like intermolecular coupling in conjugated aromatic systems [10]. In pyrene-based semiconductors, blue-shifted PL emission is frequently associated with

more localized excited-state recombination and comparatively reduced aggregation-assisted energy relaxation pathways [31]. The relatively sharp and intense emission profile observed for Py-2 therefore suggests more homogeneous intermolecular organization and limited aggregation-induced electronic delocalization.

In contrast, Py-1, Py-3, and Py-4 exhibited broader green-yellow emission bands centered approximately at 548, 562, and 543 nm, respectively. Such broadened and red-shifted emission features are commonly associated with changes in intermolecular excited-state interactions and aggregation-dependent relaxation processes in conjugated aromatic systems [32,33]. The particularly red-shifted emission of Py-3 therefore suggests pronounced intermolecular excited-state interactions, although the PL response alone cannot establish a specific molecular packing or π–π stacking geometry.

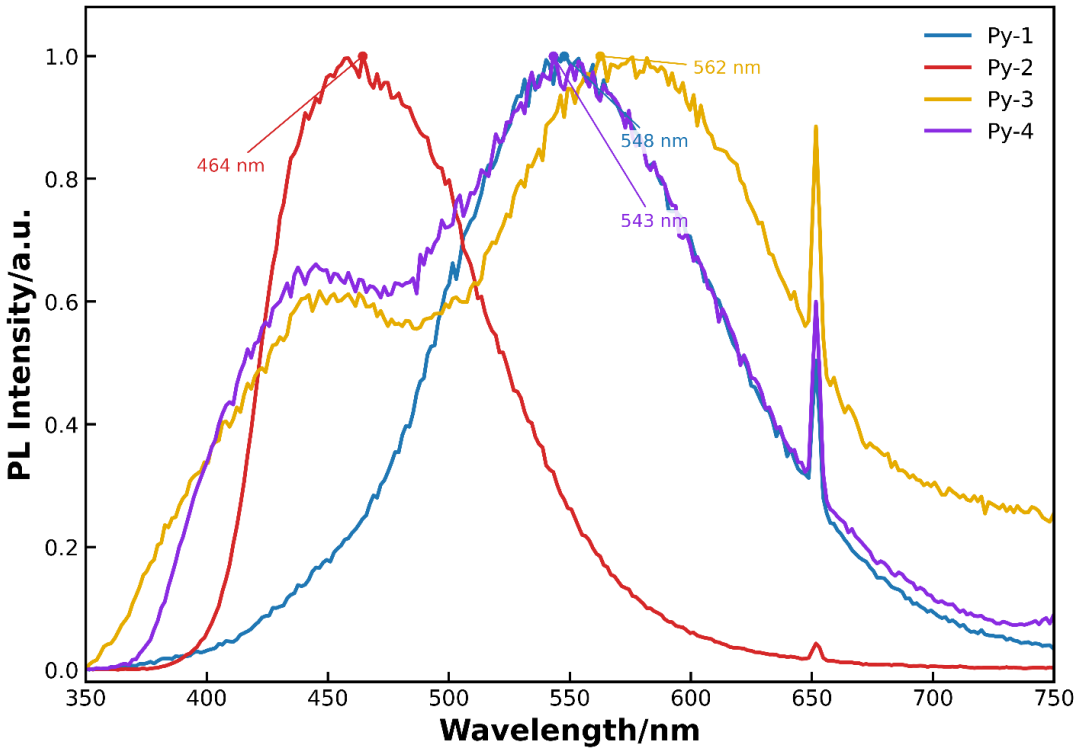


Figure 4. Photoluminescence (PL) spectra of the synthesized pyrene-based semiconducting derivatives (Py-1, Py-2, Py-3, and Py-4) were measured under 325 nm laser excitation. Distinct emission behaviors were observed as a function of the molecular substituent structure, indicating significant variations in intermolecular electronic interactions and excited-state relaxation dynamics. Py-2 exhibited a pronounced blue-shifted emission centered at approximately 464 nm, suggesting relatively reduced intermolecular aggregation and more localized excited-state recombination. In contrast, Py-1, Py-3, and Py-4 displayed broader green-yellow emission bands centered near 548, 562, and 543 nm, respectively, consistent with more pronounced intermolecular excited-state

interactions and aggregation-associated relaxation. The broader emission profiles observed for Py-3 and Py-4 indicate a wider distribution of emissive environments. Overall, the PL analyses confirm that molecular substituent engineering strongly influences excited-state electronic transitions, intermolecular coupling behavior, and radiative recombination characteristics in the pyrene-based semiconductor systems.

More importantly, Py-3 exhibited the broadest and most extended emission profile among the investigated derivatives. Such spectral broadening can arise from a broader distribution of emissive environments and multiple excited-state relaxation pathways in π-conjugated semiconductors [22]. The broad low-energy emission tail observed for Py-3 is therefore consistent with increased heterogeneity in the excited-state electronic environment and is considered together with the independent SEM and AFM observations rather than being used to assign a specific intermolecular packing arrangement. [22]

Py-4 also displayed relatively broad visible-region emission accompanied by moderate spectral broadening, consistent with pronounced aggregation-associated excited-state interactions and a heterogeneous emissive environment. Although enhanced aggregation can strengthen intermolecular electronic coupling, excessive clustering may simultaneously induce localized excited-state trapping and nonuniform radiative recombination behavior. [6,32] This interpretation is qualitatively consistent with the AFM observations, which reveal densely distributed aggregated nanodomains and pronounced topographical protrusions for Py-4.

Overall, the PL analyses clearly demonstrate that molecular substituent engineering strongly modifies intermolecular electronic coupling, aggregation characteristics, and excited-state relaxation behavior within the synthesized pyrene-based semiconductor systems. The observed substituent-dependent emission evolution further confirms that intermolecular packing organization and aggregation-assisted electronic interaction play critical roles in determining optoelectronic response and charge-transport behavior in OFET applications. [5,33]

3.5. Molecular Electronic Structure and Hole-Transport Energetics

Density functional theory calculations reveal pronounced substituent-dependent modulation of the molecular electronic structure across the Py-1–Py-4 series. At the B3LYP/6-31G(d,p) level, the calculated HOMO energies of the optimized neutral molecules were −5.458, −5.508, −5.234, and −5.528 eV for Py-1, Py-2, Py-3, and Py-4, respectively, while the corresponding LUMO energies

were −2.167, −2.066, −1.396, and −2.395 eV. The resulting Kohn–Sham HOMO–LUMO gaps were 3.292, 3.442, 3.839, and 3.133 eV, respectively. Among the investigated derivatives, Py-3 therefore exhibits the highest-lying calculated HOMO (−5.234 eV), whereas Py-4 shows the smallest calculated Kohn–Sham gap (3.133 eV). Importantly, these calculated gas-phase molecular orbital energies are used here to compare intrinsic substituent-dependent electronic trends rather than as direct equivalents of the electrochemically estimated energy levels obtained from thin-film cyclic-voltammetry measurements.

To evaluate the energetic cost of hole formation beyond the neutral-state frontier-orbital picture, the radical cations of Py-1–Py-4 were independently optimized and the corresponding IP_{ad} were determined from the total-energy differences between the optimized cationic and neutral states. The calculated IP_{ad} values were 6.688, 6.886, 6.447, and 6.878 eV for Py-1, Py-2, Py-3, and Py-4, respectively. A particularly notable result is obtained for Py-3, which exhibits the lowest IP_{ad} of the series, approximately 0.24–0.44 eV lower than those of the other derivatives. This trend is consistent with its comparatively high-lying calculated HOMO and indicates a lower intrinsic energetic cost for oxidation and formation of the positively charged molecular state. Nevertheless, ionization energetics alone cannot establish the efficiency of long-range field-effect transport, which additionally depends on structural relaxation, intermolecular electronic coupling, film organization, and charge injection at the electrode/semiconductor interface [12].

The internal hole reorganization energies provide an additional molecular-level descriptor of the structural relaxation accompanying oxidation. The calculated λ_h values were 0.251, 0.178, 0.186, and 0.185 eV for Py-1, Py-2, Py-3, and Py-4, respectively. Py-1 therefore exhibits the largest intramolecular reorganization penalty, whereas Py-2, Py-3, and Py-4 form a comparatively narrow low-λ_h group. Notably, Py-2 shows the lowest calculated λ_h (0.178 eV), while the values obtained for Py-3 and Py-4 are nearly identical (0.186 and 0.185 eV, respectively). This ordering does not reproduce the experimental field-effect mobility sequence, Py-3 > Py-4 > Py-2 > Py-1. Consequently, intramolecular reorganization energy alone cannot account for the device-level transport hierarchy. Instead, the results indicate that a comparatively low molecular relaxation penalty constitutes only one component of favorable hole transport, while the extent to which this intrinsic molecular characteristic is translated into transistor performance depends additionally on intermolecular organization, mesoscale connectivity, interfacial trapping, and contact- and channel-related resistance [12].

Table 3.1. Calculated molecular electronic and hole-transport parameters of Py-1–Py-4 at the B3LYP/6-31G (d, p) level.

Compound	HOMO (eV)	LUMO (eV)	ΔE_{KS} (eV)	IP_{ad} (eV)	λ_h (eV)
Py-1	−5.458	−2.167	3.292	6.688	0.251
Py-2	−5.508	−2.066	3.442	6.886	0.178
Py-3	−5.234	−1.396	3.839	6.447	0.186
Py-4	−5.528	−2.395	3.133	6.878	0.185

Note: HOMO and LUMO energies and the corresponding Kohn–Sham gap ΔE_{KS} were obtained from the optimized neutral molecules. IP_{ad} denotes the adiabatic ionization potential calculated from independently optimized neutral and radical-cation states, whereas λ_h represents the internal hole reorganization energy obtained using the four-point approach. The calculated gas-phase molecular quantities are used for comparative analysis within the Py-1–Py-4 series and should not be interpreted as direct equivalents of the electrochemically derived thin-film energy levels.

The combined computational results are particularly informative for distinguishing intrinsic molecular energetics from solid-state and device-level effects. Py-3 combines the lowest IP_{ad} (6.447 eV) with a relatively low λ_h (0.186 eV), providing favorable molecular-level energetics for hole formation without an unusually large structural-relaxation penalty. However, the nearly identical λ_h values of Py-3 and Py-4, together with the even lower value calculated for Py-2, demonstrate that the superior transistor response of Py-3 cannot be assigned to a single molecular energetic descriptor. Instead, the computational results establish the intrinsic energetic component of the transport picture, while the pronounced differences in experimental OFET performance must additionally reflect how the individual molecular structures organize within the solid-state films and at the relevant device interfaces. This distinction provides the basis for the morphology and electrical analyses discussed in the following sections.

3.6. X-ray Diffraction and Solid-State Organization

The solid-state organization of Py-1–Py-4 was examined by XRD using Cu Kα radiation (λ = 1.5406 Å), and the normalized, vertically offset diffraction profiles are presented in Figure 5. Each derivative exhibits a distinct set of reflections, demonstrating that peripheral substitution substantially modifies the solid-state structural organization and degree of ordering within the pyrene-based materials. The peak positions, interplanar spacings, FWHM values, and Scherrer-derived apparent coherent-domain sizes are summarized in Table 3.2. Reported Scherrer sizes are apparent coherence lengths; without a documented instrumental-line-broadening correction, they should not be interpreted as absolute crystallite sizes.

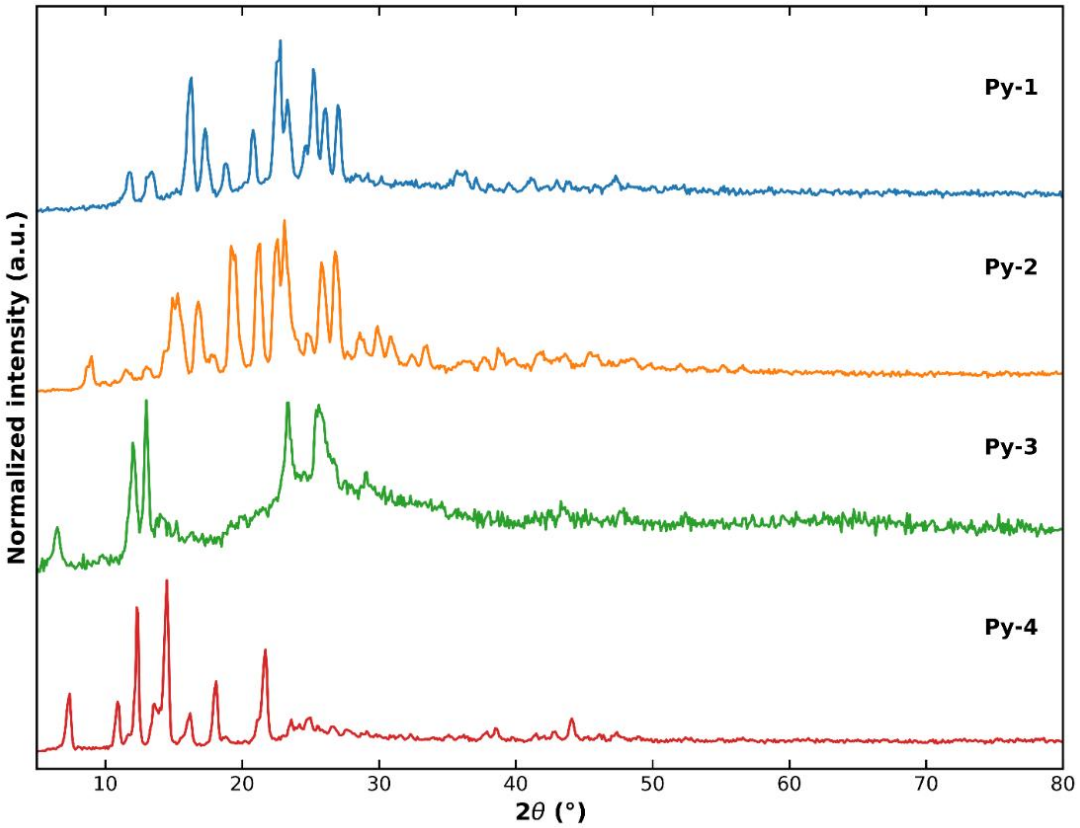


Figure 5. Normalized and vertically offset X-ray diffraction patterns of Py-1–Py-4 recorded using Cu Kα radiation (λ = 1.5406 Å). The profiles are plotted over the common 2θ range of 5–35° to highlight substituent-dependent differences in low- and intermediate-angle molecular organization.

Py-1 displays reflections at 2θ = 16.3°, 17.3°, 20.8°, 22.8°, 25.2°, 26.1°, and 27.0°, corresponding to d-spacings of 0.543–0.330 nm. The derived apparent coherent-domain sizes are 12.7–20.6 nm, with a mean value of approximately 17.8 nm. The multiple intermediate-angle reflections indicate

appreciable molecular ordering, while their differing widths point to a nonuniform distribution of ordered domains.

Py-2 exhibits the most complex intermediate-angle pattern, with reflections at 15.3°, 16.8°, 19.2°, 21.3°, 22.6°, 23.1°, 25.8°, and 26.8°. The corresponding d-spacings extend from 0.579 to 0.332 nm. Most Scherrer-derived sizes fall between approximately 8 and 24 nm. Because the 22.6° and 23.1° components overlap strongly, the FWHM and domain-size estimate assigned to 23.1° should be treated as approximate rather than as an independently resolved crystallographic value.

Py-3 shows a simpler profile consisting of low-angle reflections at 12.0° and 13.0° together with broader features at 23.4° and 25.6°. The low-angle peaks correspond to relatively large periodic spacings of 0.737 and 0.680 nm and yield apparent coherent-domain sizes of 18.8 and 23.3 nm, respectively. In contrast, the broader high-angle features yield smaller values of 9.7 and 8.6 nm. This coexistence of a defined low-angle periodicity and broader short-range correlations distinguishes the solid-state structural organization of Py-3 from that of Py-1 and Py-2.

Py-4 is distinguished by pronounced low-angle reflections at 7.4°, 10.9°, 12.3°, and 14.5°, followed by features at 18.1° and 21.7°. The 7.4° reflection corresponds to the largest d-spacing in the series (1.194 nm), indicating a long periodic molecular spacing. The narrow 12.3° peak (FWHM = 0.255°) gives an apparent coherent-domain size of 31.3 nm, the largest individual value obtained among the four derivatives. The mean apparent coherent-domain size is approximately 22.5 nm for Py-4, compared with 17.8, 13.9, and 15.1 nm for Py-1, Py-2, and Py-3, respectively.

Table 3.2. XRD peak parameters and Scherrer-derived apparent coherent-domain sizes of Py-1–Py-4.

Sample	2θ (°)	d (nm)	FWHM (°)	D (nm)
Py-1	16.3	0.543	0.516	15.56
	17.3	0.512	0.447	17.96
	20.8	0.427	0.401	20.16
	22.8	0.390	0.638	12.71
	25.2	0.353	0.473	17.22
	26.1	0.341	0.397	20.55

Sample	2θ (°)	d (nm)	FWHM (°)	D (nm)
	27.0	0.330	0.407	20.06
Py-2	15.3	0.579	0.981	8.17
	16.8	0.527	0.599	13.41
	19.2	0.462	0.648	12.43
	21.3	0.417	0.523	15.46
	22.6	0.393	0.333	24.30
	23.1	0.385	1.267	6.40*
	25.8	0.345	0.521	15.66
	26.8	0.332	0.527	15.50
Py-3	12.0	0.737	0.424	18.83
	13.0	0.680	0.344	23.25
	23.4	0.380	0.835	9.71
	25.6	0.348	0.943	8.64
Py-4	7.4	1.194	0.392	20.30
	10.9	0.811	0.346	23.07
	12.3	0.719	0.255	31.29
	14.5	0.610	0.386	20.72
	18.1	0.490	0.392	20.50
	21.7	0.409	0.428	18.91

**The Py-2 feature at 23.1° overlaps strongly with the adjacent 22.6° reflection; its FWHM and D values are therefore approximate. D values were calculated using $K = 0.9$ and $\lambda = 0.15406$ nm.*

The average coherent-domain-size sequence (Py-4 > Py-1 > Py-3 > Py-2) does not reproduce the field-effect mobility sequence (Py-3 > Py-4 > Py-2 > Py-1). Thus, the Scherrer-derived size alone is insufficient to explain charge transport. The superior device response of Py-3 is instead consistent with a balance among its distinct solid-state structural organization, interconnected film morphology,

interdomain connectivity, and reduced electrically active trapping. The XRD results therefore provide a structural link between molecular substitution and solid-state organization, which is considered together with the SEM, AFM, electrical, and OFET results in the following sections.

3.7. Surface Morphology Analysis

The surface morphologies of the synthesized pyrene-based semiconductor derivatives were investigated using SEM and AFM, and the obtained results are presented in Figures 6 and 7, respectively. The combined SEM and AFM analyses revealed a pronounced substituent-dependent evolution in microstructural organization, aggregation behavior, and nanoscale surface topology within the pyrene-based semiconductor films.

As shown in the SEM images in Figure 6, Py-1 exhibited a relatively compact, featureless surface morphology with limited long-range structural organization. Such comparatively smooth and homogeneous surface characteristics generally indicate a comparatively low degree of mesoscale surface organization and limited formation of interconnected morphological domains in conjugated organic semiconductor systems. [1,2] The absence of pronounced interconnected domains additionally suggests limited charge-percolation pathways across the film surface.

In contrast, Py-2 and Py-3 exhibited interconnected fibrillar and network-like microstructures distributed across the semiconductor surface. The emergence of these elongated, partially aligned morphological domains indicates enhanced mesoscale organization and increased connectivity of the semiconductor domains within the conjugated pyrene framework. [3,5] Particularly for Py-3, the highly interconnected fibrillar morphology provides a surface organization that is favorable for continuous lateral charge transport. Although SEM does not directly resolve molecular π–π stacking, the increased connectivity of the observed domains is consistent with a morphology that supports more continuous carrier-transport pathways [3,9].

Py-4 exhibited comparatively larger aggregated domains accompanied by irregular clustered surface features, indicating substantial intermolecular aggregation and increased local aggregation density. Although stronger aggregation may enhance intermolecular electronic communication, excessive clustering can simultaneously induce local transport nonuniformity and grain-boundary-assisted carrier trapping behavior [6]. The formation of densely aggregated domains therefore suggests that

excessive aggregation may partially disrupt homogeneous charge transport despite increased local intermolecular interactions.

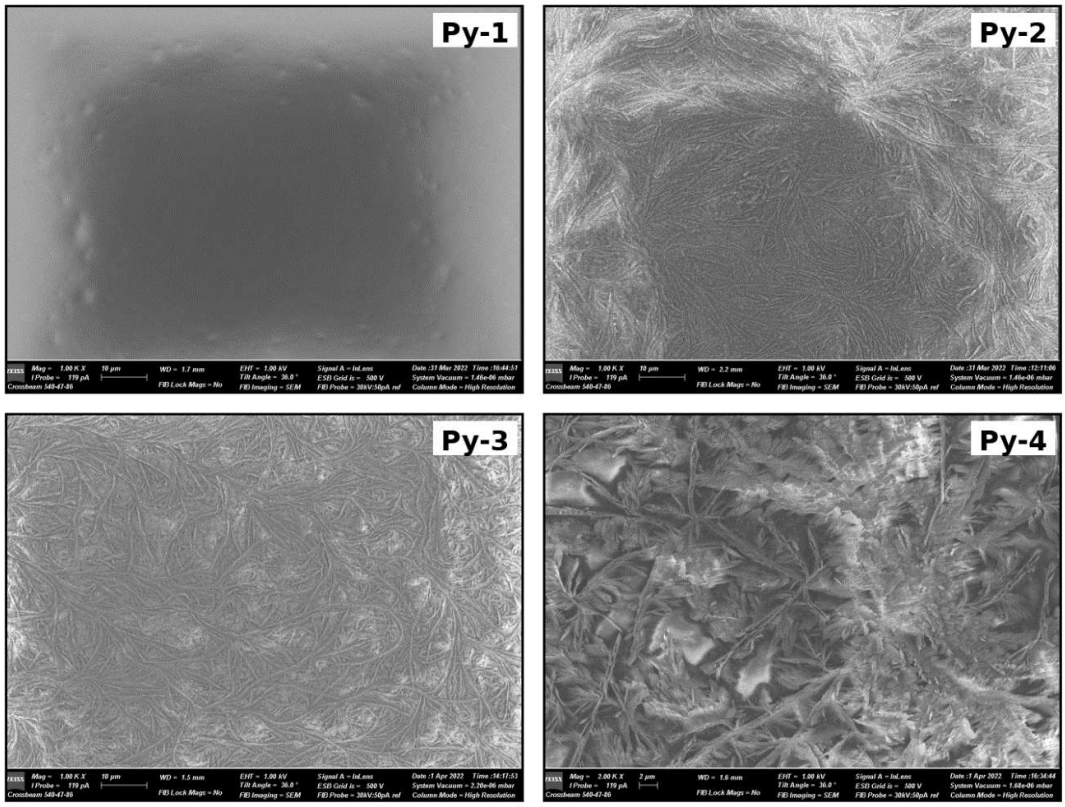


Figure 6. SEM surface morphologies of the synthesized pyrene derivatives: (a) Py-1, (b) Py-2, (c) Py-3, and (d) Py-4. Distinct substituent-dependent morphological evolution was observed across the pyrene-based semiconductor series, ranging from relatively smooth, compact surface organization to interconnected, fibrillar, and aggregated microstructures. The observed evolution demonstrates that molecular substitution strongly influences the mesoscale organization, connectivity, and aggregation characteristics of the semiconductor films.

The AFM analyses shown in Figure 7 further confirmed the substituent-dependent nanoscale structural evolution observed in the SEM measurements. Py-1 exhibited relatively low surface roughness together with homogeneous topographical distribution, supporting comparatively homogeneous nanoscale surface organization with limited development of pronounced interconnected morphological domains. [2] In contrast, Py-2 exhibited interconnected nanoscale domains and moderately roughened surface features, indicating enhanced nanoscale domain connectivity and a more developed surface network within the semiconductor film.

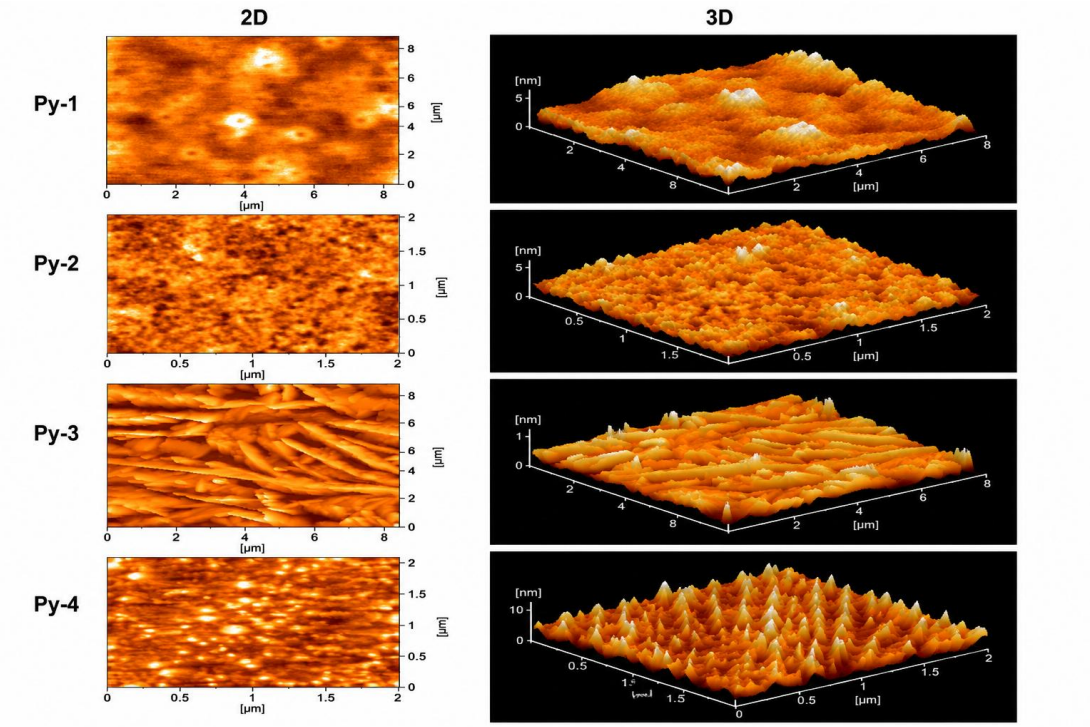


Figure 7. Two-dimensional (2D) and three-dimensional (3D) AFM surface morphologies of the synthesized pyrene-based semiconductor derivatives: Py-1, Py-2, Py-3, and Py-4. The AFM analyses reveal clear substituent-dependent differences in nanoscale surface organization. Py-1 exhibits comparatively homogeneous topography, whereas Py-2 displays interconnected granular domains. Py-3 exhibits pronounced fibrillar features and enhanced lateral connectivity across the film surface. In contrast, Py-4 shows densely distributed aggregated nanodomains and pronounced topographical protrusions, indicating increased morphological heterogeneity. These observations demonstrate that molecular substitution strongly influences nanoscale film organization and surface topology. The AFM results are interpreted as complementary morphological evidence and are not used independently to assign specific π–π stacking geometries; molecular-scale structural organization is considered separately on the basis of the XRD analysis presented in Section 3.6.

More pronounced morphological ordering was observed for Py-3, where elongated fibrillar domains and directionally aligned nanoscale structures became dominant across the film surface. Such fibrillar organization provides enhanced lateral domain connectivity and may facilitate more continuous charge-transport pathways within the semiconductor film [9,32]. The observed morphology therefore suggests the formation of efficient lateral charge-transport pathways that may facilitate carrier mobility in OFET architectures.

On the other hand, Py-4 exhibited densely distributed aggregated nanodomains together with sharp topographical protrusions and increased local surface roughness. The formation of these spike-like

morphological features indicates pronounced molecular clustering and a heterogeneous distribution of nanoscale surface organization within the semiconductor film. [6,22] Such nonuniform aggregation behavior may introduce localized transport barriers and trap-assisted carrier scattering despite enhanced intermolecular electronic coupling.

Overall, the combined SEM and AFM analyses demonstrate that molecular substituent engineering strongly influences nanoscale film organization, surface morphology, and aggregation behavior within the pyrene-based semiconductor series. These morphology-dependent variations are consistent with the systematic differences in charge-transport characteristics subsequently observed in the corresponding OFET devices [3,9].

3.9. OFET Characteristics

The charge-transport characteristics of the synthesized pyrene derivatives were systematically evaluated in top-gate/bottom-contact OFET architectures using patterned ITO source/drain electrodes, the respective Py-1–Py-4 semiconductor layers, PiBMA as the gate dielectric, and thermally evaporated Al gate electrodes. The output characteristics of the resulting devices are presented in Figure 8. All four derivatives showed a clear increase in the magnitude of the drain current as the gate bias became increasingly negative, confirming p-channel field-effect operation. This p-channel electrical response is consistent with the positive field-effect independently obtained for all four semiconductor films in Section 3.8, providing complementary support for hole-dominant transport across the Py-1–Py-4 series [2,5,12].

A pronounced substituent-dependent variation in the output current was observed across the Py-1–Py-4 devices. The maximum drain-current response followed the general order Py-3 > Py-4 > Py-2 > Py-1. Importantly, this hierarchy is not independent of the structural and morphological characteristics established in the preceding sections. Py-1, which exhibited a comparatively compact and weakly organized surface morphology, produced the lowest output current. In contrast, Py-2 showed an appreciable increase in current, consistent with the development of more interconnected nanoscale domains and improved intermolecular organization. The strongest output response was obtained for Py-3, whose SEM and AFM images revealed pronounced fibrillar organization and interconnected transport pathways. Py-4 maintained relatively high current levels but did not outperform Py-3, despite its strong tendency to aggregate. This distinction indicates that increased aggregation alone is insufficient to account for the observed field-effect transport trend; instead, the

spatial organization and connectivity of the semiconductor domains appear to be important factors influencing lateral charge propagation [3,6,9].

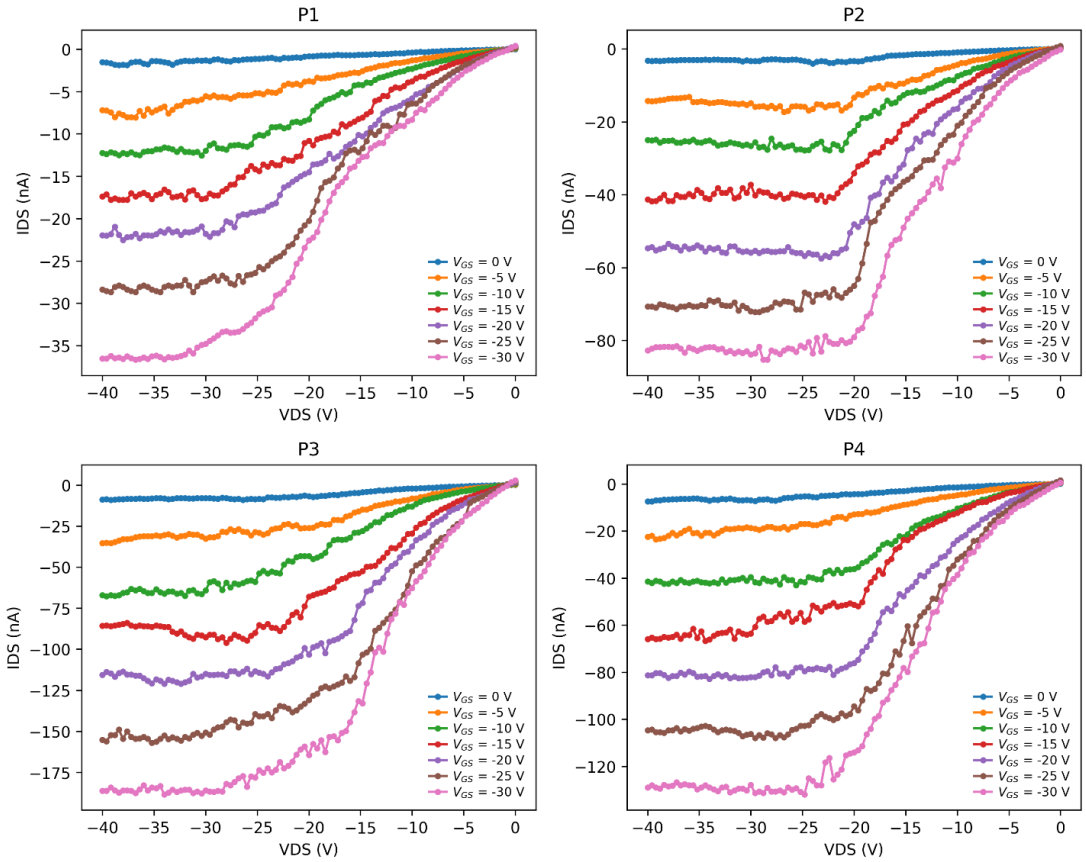


Figure 8. Output characteristics of OFET devices fabricated using Py-1, Py-2, Py-3, and Py-4 as active semiconductor layers. The output curves were recorded in the negative-bias region by sweeping the drain voltage over the negative-bias range while varying the gate bias from 0 to −30 V in 5 V intervals (as labeled in the plotted traces). All devices exhibited p-channel OFET behavior, characterized by a gradual increase in drain-current magnitude as the gate bias became more negative. Distinct differences in output current levels were observed among the pyrene derivatives, following the general order: Py-3 > Py-4 > Py-2 > Py-1. The enhanced current response of Py-3 is consistent with its more interconnected fibrillar film morphology, whereas the lower responses of Py-1 and Py-4 coincide with comparatively limited domain connectivity and more heterogeneous aggregation, respectively.

The output characteristics therefore provide electrical evidence consistent with the morphology-dependent transport trends inferred from the complementary microscopic analyses. In organic semiconductors, charge transport is highly sensitive to intermolecular orbital overlap, energetic disorder, domain connectivity, and the microstructure established at the semiconductor/dielectric and semiconductor/electrode interfaces [3,7,21]. The interconnected fibrillar morphology observed for

Py-3 provides comparatively continuous mesoscale pathways that may favor lateral hole transport. Conversely, the densely aggregated and topographically heterogeneous morphology of Py-4 may introduce localized transport barriers even when intermolecular interactions are relatively strong. Such morphology-controlled transport is well established in organic transistor systems, where improved structural connectivity can enhance effective mobility whereas excessive disorder or discontinuous aggregation can restrict long-range carrier motion [6,7].

The transfer characteristics recorded at $V_{DS} = -30$ V are shown in Figure 9 and further demonstrate substantial differences in the switching behavior of the four derivatives. Forward and backward gate-voltage sweeps revealed measurable hysteresis in all devices, although its magnitude varied strongly with molecular structure. The extracted threshold-voltage hysteresis (ΔV_{th}) decreased from 5.5 V for Py-1 to 2.9 V for Py-2 and reached a minimum of only 1.1 V for Py-3, before increasing markedly to 9.4 V for Py-4. Hysteresis in OFETs can originate from several processes, including charge trapping at the semiconductor/dielectric interface, energetic disorder within the semiconductor, mobile or dipolar species, and bias-induced trapping within structurally heterogeneous regions [5,18]. Accordingly, the exceptionally small hysteresis observed for Py-3 is consistent with comparatively stable electrostatic channel modulation and a lower contribution from bias-dependent trapping processes. In contrast, the pronounced hysteresis of Py-4 is consistent with its more heterogeneous film morphology and suggests a greater contribution from localized trapping environments.

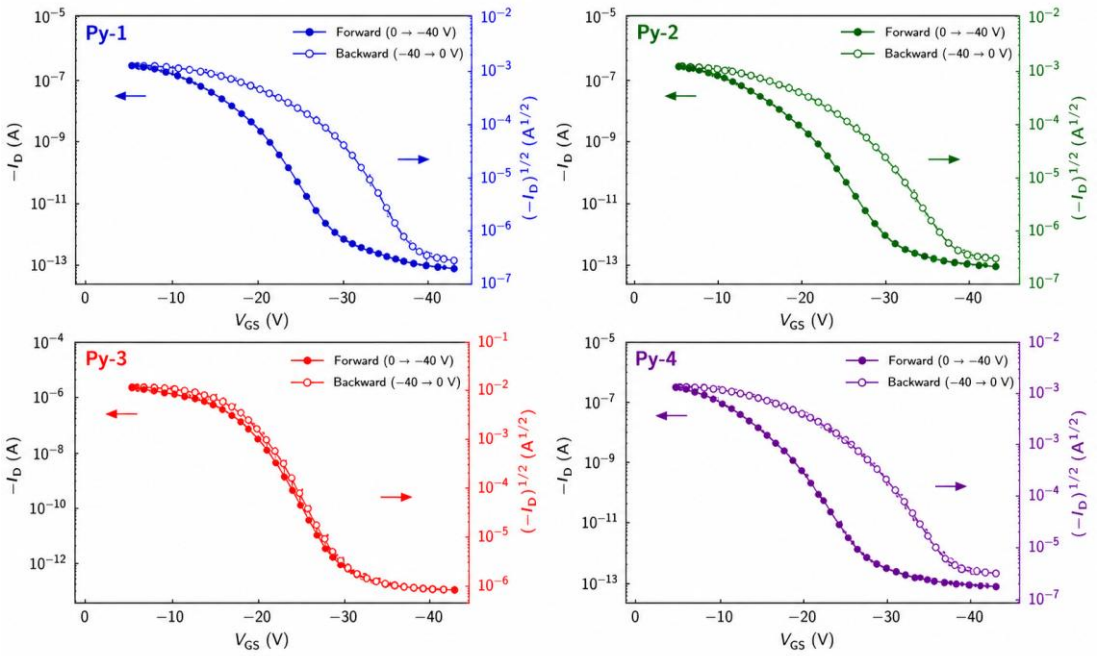


Figure 9. Transfer characteristics of the OFET devices based on Py-1, Py-2, Py-3, and Py-4 semiconductor layers measured at a constant drain voltage of V_{DS} = −30 V. The transfer curves were recorded during forward (0 → −40 V) and backward (−40 → 0 V) gate-voltage sweeps to evaluate the p-channel switching behavior and gate-bias hysteresis of the devices. Filled and open symbols represent the forward and backward sweeps, respectively. The left axes show the drain current ($-I_D$) on a logarithmic scale, while the corresponding square-root current representation, $(-I_D)^{1/2}$, is indicated on the right axes.

The extracted field-effect parameters, summarized in Figure 10, further establish Py-3 as the best-performing semiconductor within the investigated series. The field-effect mobility increased by almost two orders of magnitude from 6.9 × 10^{-3} cm^2 V^{-1} s^{-1} for Py-1 to 5.4 × 10^{-1} cm^2 V^{-1} s^{-1} for Py-3. Py-2 exhibited an intermediate mobility of 9.3 × 10^{-2} cm^2 V^{-1} s^{-1}, whereas Py-4 reached 2.25 × 10^{-1} cm^2 V^{-1} s^{-1}. The resulting mobility sequence, Py-3 > Py-4 > Py-2 > Py-1, closely follows the output-current hierarchy and supports a systematic relationship between substituent-dependent film organization and effective field-effect transport.

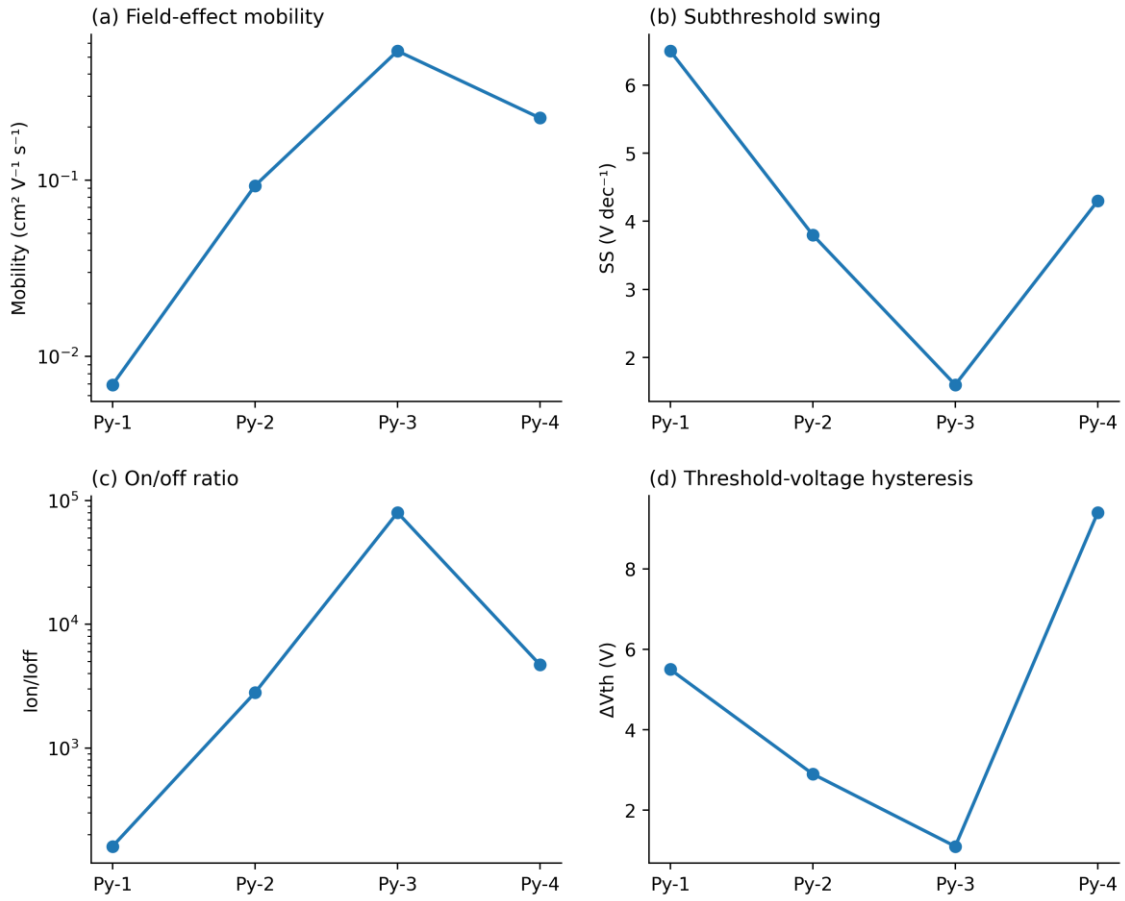


Figure 10. Comparative evolution of the extracted OFET parameters for the Py-1–Py-4 semiconductor series: (a) field-effect mobility (μFE), (b) subthreshold swing (SS), (c) current on/off ratio (Ion/Ioff), and (d) threshold-voltage hysteresis (ΔVth). The parameter evolution illustrates the substituent-dependent variation in charge-transport and switching characteristics across the pyrene derivative series. The values shown correspond to the representative devices discussed in Section 3.9; statistical mean ± standard deviation values obtained from three independently characterized devices are reported separately in Table 3.4. Panel (a) reflects the corrected W/L = 20 geometry; panels (b–d) retain the reported non-mobility metrics.

A similarly systematic evolution was observed in the current modulation and subthreshold characteristics. The Ion/Ioff ratio increased from 1.6×10^2 for Py-1 to 2.8×10^3 for Py-2 and reached 8.0×10^4 for Py-3, before decreasing to 4.7×10^3 for Py-4. Simultaneously, the subthreshold swing decreased from 6.5 V dec^{-1} for Py-1 to 3.8 V dec^{-1} for Py-2 and reached its minimum value of 1.6 V dec^{-1} for Py-3, whereas Py-4 exhibited a higher SS of 4.3 V dec^{-1}. Thus, Py-3 simultaneously combines the highest field-effect mobility, the largest current on/off ratio, the lowest subthreshold swing, and the smallest threshold-voltage hysteresis. This concurrent improvement across several

independent transistor metrics is particularly significant because it demonstrates that the superior behavior of Py-3 cannot be attributed simply to an increase in absolute drain current.

The threshold-voltage behavior provides further insight into the effect of molecular structure on channel formation. The forward-sweep Vth shifted from −12.7 V for Py-1 to −8.2 V for Py-2 and −4.9 V for Py-3, indicating progressively easier formation of the accumulated hole channel. Py-4 exhibited V_{th} = −9.6 V, demonstrating a partial reversal of this trend. Threshold voltage in organic transistors is influenced by several coupled factors, including semiconductor/dielectric interfacial trap density, energetic disorder, charge injection, and molecular organization [5,18,34]. The comparatively small magnitude of Vth for Py-3, together with its low SS and minimal hysteresis, therefore supports a more favorable interfacial and transport environment rather than merely stronger intermolecular aggregation.

The behavior of Py-4 is particularly informative for establishing the structure–property relationship. Although Py-4 exhibits higher mobility and output current than Py-1 and Py-2, its substantially larger ΔV_{th} and increased SS indicate that its stronger aggregation does not translate into correspondingly improved switching quality. This observation supports a distinction between beneficial molecular organization and excessive aggregation. Strong intermolecular interactions can facilitate electronic coupling, but heterogeneous clustering can simultaneously increase energetic disorder and trapping, producing a device that carries relatively high current while exhibiting inferior gate control. The Py-3/Py-4 comparison therefore supports the interpretation that favorable OFET performance in this molecular series is associated with a balance among intermolecular interactions, morphological connectivity, and interfacial uniformity, rather than with aggregation strength alone.

Field-effect mobilities were recalculated for the confirmed channel dimensions (W = 1000 μm and L = 50 μm) using the previously extracted transfer-fit slopes and the estimated C_{ox}. The resulting values should be interpreted in light of the capacitance uncertainty and the absence of an independent re-fit of the raw transfer curves.

This interpretation is particularly important because apparent field-effect mobility in OFETs can be strongly influenced by charge injection and contact resistance. Poor semiconductor/electrode contacts can suppress drain current, distort transfer and output characteristics, shift the apparent threshold voltage, and lead to underestimation or misinterpretation of intrinsic semiconductor transport

properties [36–38]. Consequently, the mobility trend alone is insufficient to determine whether the superior performance of Py-3 stems primarily from improved channel transport, improved charge injection, or a combination of both. This distinction is addressed in the following section through channel-length-dependent transfer-length-method analysis, which independently evaluates the contact and sheet-resistance contributions across the Py-1–Py-4 series.

Overall, the OFET results establish a clear substituent-dependent transport hierarchy within the synthesized pyrene semiconductor series. The progression from Py-1 to Py-3 is characterized by increasing field-effect mobility, improved current modulation, reduced subthreshold swing, lower threshold-voltage magnitude, and progressively suppressed hysteresis. The partial deterioration observed for Py-4 demonstrates that excessive aggregation can counteract the benefits of enhanced intermolecular interaction. Taken together with the optical, XRD, electrical, SEM, and AFM results, these findings indicate that the electrical performance of the investigated pyrene OFETs is associated not simply with the presence of an extended π-conjugated framework, but with substituent-dependent differences in film organization, interfacial trapping behavior, and the continuity of lateral charge-transport pathways.

3.10. Channel-Length-Dependent Resistance and Contact Analysis

Although the transfer characteristics establish clear differences in the apparent field-effect transport of Py-1–Py-4, the extracted mobility alone cannot distinguish between resistance contributions originating from the semiconductor channel and those associated with charge injection at the source/drain contacts. This distinction is particularly important in organic field-effect transistors because contact resistance can represent a substantial fraction of the total device resistance and can consequently influence the apparent mobility, threshold behavior, and current modulation extracted from conventional transistor characteristics [37,39,40]. To independently examine these contributions, channel-length-dependent resistance measurements were therefore performed using the transfer-length method (TLM).

For the TLM analysis, a separate set of devices with a constant channel width of 1000 μm and channel lengths of 20, 50, and 100 μm was fabricated under otherwise identical processing conditions. The experimentally determined total resistances are summarized in Table 3.3. For each pyrene derivative, the total device resistance increased systematically with increasing channel length, demonstrating the

expected contribution of the semiconductor channel to the overall device resistance. At all investigated channel lengths, Py-1 exhibited the highest Rtot, whereas Py-3 consistently displayed the lowest resistance. At L = 20 µm, for example, Rtot decreased from 587 MΩ for Py-1 to 291 MΩ for Py-2, 126 MΩ for Py-3, and 190 MΩ for Py-4. The same resistance hierarchy was retained at L = 100 µm, with Rtot values of 893, 480, 218, and 334 MΩ for Py-1, Py-2, Py-3, and Py-4, respectively. The resulting resistance sequence, Py-3 < Py-4 < Py-2 < Py-1, is therefore the inverse of the field-effect mobility and output-current trends established in Section 3.9.

Table 3.3. Channel-length-dependent total resistance (Rtot) values of OFETs based on Py-1, Py-2, Py-3, and Py-4 semiconductor layers measured at identical channel width and device-fabrication conditions.

Device	**L (µm)**	**W (µm)**	**R_{tot} (MΩ)**
Py-1	20	1000	587
Py-1	50	1000	703
Py-1	100	1000	893
Py-2	20	1000	291
Py-2	50	1000	359
Py-2	100	1000	480
Py-3	20	1000	126
Py-3	50	1000	156
Py-3	100	1000	218
Py-4	20	1000	190
Py-4	50	1000	237
Py-4	100	1000	334

Within the conventional TLM framework, the channel-length dependence of the total resistance can be expressed as

$$R_{tot}(L) = 2R_c + (R_{sh}/W)L \quad (5)$$

where Rc is the contact resistance associated with a single source/drain contact, R_{sh} is the semiconductor sheet resistance, W is the channel width, and L is the channel length [39,41].

Accordingly, linear fitting of R_{tot} as a function of L yields an intercept corresponding to $2R_c$, whereas the slope corresponds to R_{sh}/W.

Interpretation of these regression-derived resistances is restricted to comparisons among the reported devices. With only three channel lengths per semiconductor and no raw resistance uncertainties, the fits do not establish contact-resistance uncertainty or separate microscopic injection barriers from morphology-dependent channel effects.

The channel-length-dependent resistance data in Table 3.3 were re-evaluated by ordinary least-squares regression using the three reported lengths (20, 50 and 100 µm). The resulting coefficients of determination are 0.99998, 0.99971, 0.99700 and 0.99703 for Py-1, Py-2, Py-3 and Py-4, respectively. These fits provide a consistent comparison within the reported three-point dataset, but the limited number of lengths and absence of uncertainty estimates restrict the precision of the extracted contact resistances.

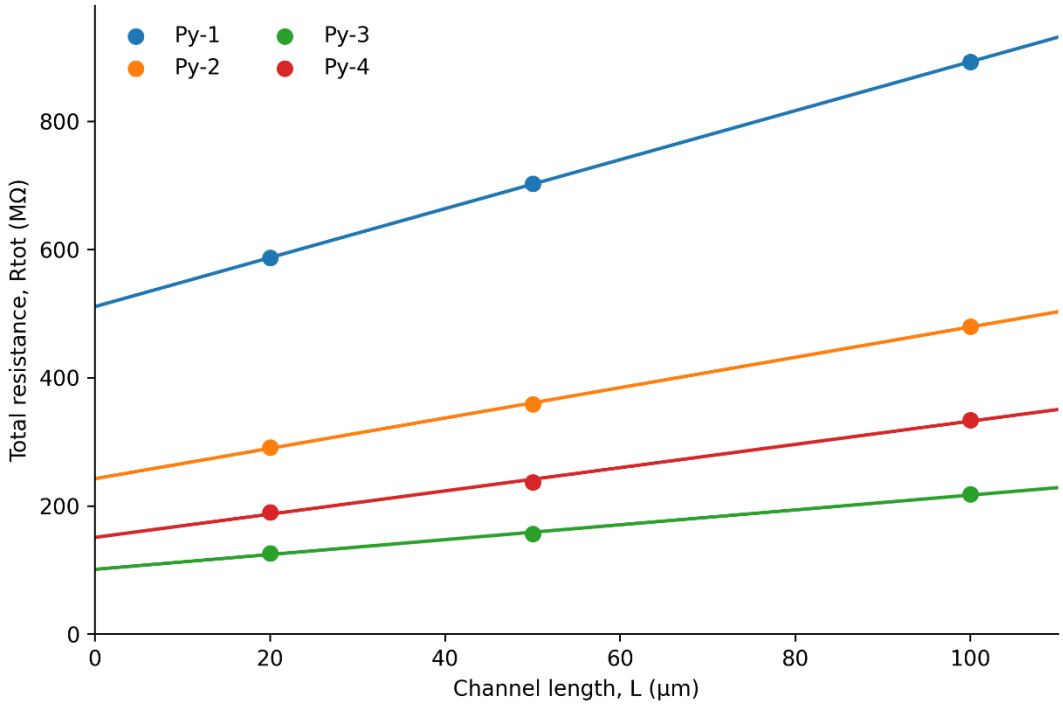


Figure 11. Channel-length dependence of the total resistance of Py-1–Py-4 OFETs at L = 20, 50, and 100 µm. Symbols show the resistance values reported in Table 3.3, and solid lines show independently recalculated ordinary least-squares fits. Extracted resistance parameters are summarized in Table 3.3.

The recomputed regression parameters are summarized in Table 3.3. The extracted single-contact resistances (Rc) are 255.53, 121.23, 50.49 and 75.43 MΩ for Py-1, Py-2, Py-3 and Py-4, respectively. The corresponding sheet resistances (Rsh) are 3822, 2368, 1159 and 1814 MΩ sq^{-1}. Py-3 therefore retains the lowest estimated contact and sheet resistances within the investigated series. These values are calculated from the tabulated total resistances rather than independently recovered raw I–V measurements. Because only three channel lengths were available, the fits are descriptive and do not establish bias-independent or geometry-independent contact resistances. Contact and sheet resistance estimates apply to the measurement conditions used for the tabulated Rtot values.

Table 3.4. Contact resistance (Rc), sheet resistance (Rsh), and linear regression parameters extracted from the TLM analysis of Py-1, Py-2, Py-3, and Py-4-based OFETs. Values recalculated from Table 3.3 by three-point least-squares fitting; rounded to shown precision.

Device	2Rc (MΩ)	Rc (MΩ)	Rsh (MΩ sq^{-1})	R^2
Py-1	511.06	255.53	3822	1.0000
Py-2	242.46	121.23	2368	0.9997
Py-3	100.98	50.49	1159	0.9970
Py-4	150.86	75.43	1814	0.9970

The simultaneous reduction of Rc and Rsh for Py-3 is particularly significant. The lower R_{sh} indicates that the enhanced OFET response of Py-3 cannot be associated solely with differences in charge injection at the ITO/semiconductor contacts; reduced resistance within the semiconductor channel also contributes to the observed transport enhancement. At the same time, the reduction in Rc indicates a more favorable effective injection environment at the patterned ITO/Py-3 interface. Contact resistance in OFETs is sensitive to energetic alignment, molecular orientation near the electrode, local semiconductor morphology, injection barriers, and the ability of injected carriers to access the accumulated transport channel [36,37,40]. Because the electrode material, channel width, dielectric system, and fabrication procedure were maintained across the Py-1–Py-4 series, the systematic variation in Rc is consistent with substituent-dependent differences in the semiconductor film and its organization near the electrode interface rather than changes in the electrode material itself.

The TLM results are therefore highly consistent with the morphological evolution revealed by SEM and AFM. The comparatively compact, weakly interconnected morphology of Py-1 is accompanied by both high channel and high contact resistance. Py-2 develops more interconnected domains and consequently exhibits intermediate Rsh and Rc values. In contrast, the pronounced fibrillar organization of Py-3 provides a plausible structural basis for its substantially reduced sheet resistance by creating more continuous lateral transport pathways through the semiconductor layer. The same interconnected organization may also favor electronic connectivity between the patterned ITO electrodes and adjacent semiconductor domains, thereby being consistent with the lower R_c obtained for Py-3. Such strong dependence of contact and channel transport on molecular packing and interfacial microstructure is well established in organic transistor systems [5,36,37,42].

The behavior of Py-4 again provides an instructive contrast. Despite exhibiting stronger aggregation and a relatively high drain current, both R_c and R_{sh} increase compared with Py-3. This result reinforces the conclusion from the transfer characteristics that stronger aggregation does not necessarily imply more efficient long-range charge transport. The heterogeneous clustered morphology observed for Py-4 may maintain substantial local intermolecular electronic coupling while simultaneously introducing discontinuities, localized barriers, and trapping environments that impede carrier propagation across larger length scales. The increase in R_{sh} from 1159 MΩ sq^{-1} for Py-3 to 1814 MΩ sq^{-1} for Py-4 is consistent with this interpretation, while the accompanying increase in Rc from 50.49 to 75.43 MΩ suggests that the same morphological heterogeneity may also influence charge injection and extraction near the electrode interface.

Most importantly, the TLM analysis reproduces the same transport hierarchy observed in the conventional OFET characteristics. This agreement between complementary electrical metrics strengthens the association between the observed performance differences and substituent-dependent film organization and transport connectivity. Py-3 combines the highest field-effect mobility and I_{on}/I_{off} ratio with the lowest SS and hysteresis, while simultaneously exhibiting the lowest R_c and R_{sh}. Conversely, Py-1 exhibits the poorest field-effect performance together with the largest contact and sheet resistances.

Overall, the channel-length-dependent resistance analysis demonstrates systematic substituent-dependent differences in both contact- and channel-related resistance contributions across the pyrene-based OFET series. The superior field-effect response of Py-3 is accompanied by simultaneous

reductions in contact resistance and semiconductor sheet resistance, whereas the partial deterioration observed for Py-4 coincides with increases in both quantities. These results provide a quantitative electrical link between nanoscale film organization and macroscopic transistor characteristics and establish an additional basis for the structure–morphology–transport correlation developed in the following sections.

3.11. Statistical Analysis and Device Reproducibility

To assess whether the substituent-dependent transport trends identified from the representative OFET characteristics were reproducible across independently fabricated devices, statistical analysis was performed on three transistors per pyrene semiconductor (n = 3). The extracted field-effect mobility, threshold voltage, subthreshold swing, current on/off ratio, and threshold-voltage hysteresis are summarized in Table 3.5 as mean ± standard deviation. Statistical evaluation of multiple devices is particularly important for solution-processed OFETs because local variations in semiconductor morphology, molecular orientation, film thickness, and electrode/channel interfaces can introduce appreciable device-to-device variation in the extracted electrical parameters [43-45].

Table 3.5. Statistical summary of the electrical parameters extracted from independently fabricated Py-1-, Py-2-, Py-3-, and Py-4-based OFET devices. The field-effect mobility, threshold voltage, subthreshold swing, current on/off ratio, and threshold-voltage hysteresis are presented as mean ± standard deviation for three independently characterized devices (n = 3).

Device	μ_{FE} ($cm^2\ V^{-1}\ s^{-1}$)	V_{th} (V)	SS ($V\ dec^{-1}$)	I_{on}/I_{off}	ΔV_{th} (V)
Py-1	$(6.81 \pm 0.51) \times 10^{-3}$	-12.7 ± 0.6	6.4 ± 0.4	$(1.60 \pm 0.15) \times 10^{2}$	5.4 ± 0.4
Py-2	$(9.33 \pm 0.60) \times 10^{-2}$	-8.2 ± 0.4	3.7 ± 0.3	$(2.80 \pm 0.25) \times 10^{3}$	2.9 ± 0.3
Py-3	$(5.43 \pm 0.33) \times 10^{-1}$	-4.9 ± 0.3	1.7 ± 0.1	$(8.00 \pm 0.65) \times 10^{4}$	1.2 ± 0.1
Py-4	$(2.244 \pm 0.162) \times 10^{-1}$	-9.6 ± 0.5	4.3 ± 0.3	$(4.70 \pm 0.40) \times 10^{3}$	9.3 ± 0.6

The statistical results demonstrate that the transport hierarchy established from the representative devices is retained across independently fabricated transistors. Py-1 exhibited the lowest mean field-

effect mobility (6.81 ± 0.51) × 10^{-3} cm^2 V^{-1} s^{-1}, whereas Py-2 showed an increase of more than one order of magnitude to (9.33 ± 0.60) × 10^{-2} cm^2 V^{-1} s^{-1}. The highest mean mobility was obtained for Py-3, reaching (5.43 ± 0.33) × 10^{-1} cm^2 V^{-1} s^{-1}, while Py-4 exhibited an intermediate value of (2.244 ± 0.162) × 10^{-1} cm^2 V^{-1} s^{-1}. Thus, the mobility sequence Py-3 > Py-4 > Py-2 > Py-1 is preserved across the independently characterized devices, demonstrating that the performance enhancement observed for Py-3 is not attributable to an isolated high-performing transistor.

The relatively small standard deviations in μ_{FE} further indicate satisfactory device-to-device consistency within each molecular system. Based on the mean and standard-deviation values, the relative standard deviation of mobility is approximately 7.5% for Py-1, 6.4% for Py-2, 6.1% for Py-3, and 7.2% for Py-4. These narrow distributions are particularly relevant for solution-processed organic transistors, where morphology-dependent variability can substantially influence apparent mobility. Previous OFET studies have emphasized that reproducibility should be evaluated using device ensembles rather than relying exclusively on a single representative transistor, because replicated measurements provide a more reliable assessment of material-dependent transport performance [43,44].

A similarly reproducible trend was observed for the switching characteristics. The mean Ion/Ioff ratio increased from (1.60 ± 0.15) × 10^2 for Py-1 to (2.80 ± 0.25) × 10^3 for Py-2 and reached a maximum of (8.00 ± 0.65) × 10^4 for Py-3. Py-4 exhibited an intermediate value of (4.70 ± 0.40) × 10^3. The preservation of this hierarchy across multiple devices indicates that the superior current modulation of Py-3 is a reproducible feature of this semiconductor/device system rather than a random device-to-device fluctuation.

The statistical evolution of the subthreshold swing provides additional evidence for reproducible differences in gate control. Py-1 exhibited SS = 6.4 ± 0.4 V dec^{-1}, which decreased to 3.7 ± 0.3 V dec^{-1} for Py-2 and reached a minimum of 1.7 ± 0.1 V dec^{-1} for Py-3. Py-4 again showed partial deterioration, with SS = 4.3 ± 0.3 V dec^{-1}. Because SS is sensitive to the electrostatic quality of the semiconductor/dielectric interface and to the density and energetic distribution of electrically active trapping states, the consistently lower SS observed for Py-3 supports more effective gate modulation across independently fabricated devices [5,18].

Threshold-voltage statistics show the same systematic molecular dependence. The mean Vth shifted from −12.7 ± 0.6 V for Py-1 to −8.2 ± 0.4 V for Py-2 and −4.9 ± 0.3 V for Py-3, before shifting back to −9.6 ± 0.5 V for Py-4. The comparatively small magnitude and narrow distribution of Vth for Py-3 indicate that formation of the accumulated hole channel occurs reproducibly at lower gate bias than in the other derivatives. The simultaneous improvement of Vth, SS, and μFE is significant because these parameters probe different aspects of transistor operation and therefore provide mutually reinforcing evidence for a favorable transport and interfacial environment in the Py-3 devices.

The hysteresis statistics are particularly informative. Py-3 exhibited the smallest ΔV_{th} of only 1.2 ± 0.1 V, compared with 5.4 ± 0.4 V for Py-1 and 2.9 ± 0.3 V for Py-2. In contrast, Py-4 displayed a markedly larger ΔVth of 9.3 ± 0.6 V. This substantial and reproducible increase in hysteresis for Py-4 is consistent with its densely aggregated and topographically heterogeneous morphology observed by SEM and AFM. Charge trapping at the semiconductor/dielectric interface and within structurally disordered regions of the semiconductor is a well-established source of transfer-curve hysteresis in OFETs [5,7,18]. The reproducibility of the high ΔV_{th} observed for Py-4 therefore indicates that its pronounced hysteresis is a systematic feature of the Py-4 devices and is consistent with the heterogeneous film morphology observed by SEM and AFM rather than representing an isolated device anomaly.

Importantly, the statistical results are fully consistent with the independent TLM analysis presented in Section 3.10. Py-3, which exhibits the highest mean mobility, highest I_{on}/I_{off} ratio, lowest SS, and smallest hysteresis, simultaneously possesses the lowest contact and sheet resistances. Conversely, Py-1 exhibits the poorest transistor performance, along with the highest Rc and Rsh, while Py-4 exhibits intermediate mobility and resistance but significantly increased hysteresis. Agreement between the statistical characteristics of the device and channel-length-dependent resistance measurements substantially reduces the likelihood that the observed transport hierarchy arises from random device-to-device variability.

Device reproducibility is increasingly recognized as an important criterion in evaluating organic transistor materials, because high mobility alone does not necessarily imply a technologically reliable semiconductor system. Studies of organic thin-film transistors have demonstrated that variations in molecular orientation and crystalline-domain distribution can produce substantial fluctuations in mobility and threshold voltage, whereas controlled semiconductor organization can considerably

narrow device-to-device parameter distributions.[43,46] Accordingly, the relatively small standard deviations obtained for the present Py-1–Py-4 devices provide an additional metric for assessing the robustness of the substituent-dependent transport trends.

Overall, the statistical analysis confirms that the electrical differences observed among the four pyrene derivatives are reproducible across independently fabricated OFETs. In particular, Py-3 consistently combines enhanced field-effect mobility and current modulation with reduced subthreshold swing and hysteresis, whereas Py-4 reproducibly exhibits partial transport deterioration accompanied by substantially increased hysteresis. These results demonstrate that the observed transistor performance hierarchy is reproducibly associated with the molecular identity of the semiconductor and its corresponding film and interfacial characteristics, rather than with isolated device variation.

3.12. From Molecular Energetics and Solid-State Organization to Charge Transport

The combined computational, spectroscopic, diffraction, morphological, electrical, transistor, resistance, and statistical analyses reveal a systematic but non-trivial relationship between molecular substitution and charge transport across the Py-1–Py-4 series. The DFT results establish that favorable intrinsic molecular energetics alone do not determine device performance: although Py-2 exhibits the lowest internal hole reorganization energy (λh = 0.178 eV), Py-3 provides the highest field-effect mobility, while Py-3 and Py-4 possess nearly identical λh values (0.186 and 0.185 eV, respectively) despite markedly different switching and trapping characteristics. Rather than exhibiting a simple monotonic relationship with either a single molecular energetic descriptor or the extent of aggregation, OFET operation therefore reflects the combined influence of intrinsic oxidation/relaxation energetics, intermolecular electronic interactions, mesoscale structural connectivity, semiconductor/electrode contact characteristics, and charge trapping at the semiconductor/dielectric interface. This distinction is particularly important for π-conjugated molecular semiconductors, in which favorable molecular energetics and local electronic coupling do not necessarily translate into efficient long-range field-effect transport unless an appropriate solid-state transport network is simultaneously established [3,5,6,12].

The optical measurements provide the first indication that the electronic environment is substantially modified by molecular substitution. The absorption maxima of Py-1, Py-2, Py-3, and Py-4 were located at approximately 345, 351, 337, and 349 nm, respectively, while the corresponding PL

maxima occurred at approximately 548, 464, 562, and 543 nm. The markedly different absorption and emission responses demonstrate that modification of the pyrene framework alters both ground-state optical transitions and excited-state intermolecular interactions. Particularly noteworthy is Py-3, which exhibits the most red-shifted PL maximum and a broad low-energy emission profile despite its comparatively blue-shifted absorption maximum. Such behavior suggests that the electronic environment established after excitation differs substantially from that inferred from absorption alone and is consistent with pronounced intermolecular excited-state interactions and a broader distribution of relaxation environments in the solid-state film [22,23,32].

The calculated ionization energetics provide a complementary molecular-level perspective. Py-3 exhibits the lowest adiabatic ionization potential of the series (IP_{ad} = 6.447 eV), compared with 6.688, 6.886, and 6.878 eV for Py-1, Py-2, and Py-4, respectively. This lower intrinsic energetic cost of oxidation is consistent with favorable hole formation in Py-3; however, its translation into superior field-effect transport must be considered together with the solid-state organization of the semiconductor film.

The XRD results provide an independent structural dimension to this comparison. The four derivatives exhibit clearly distinct diffraction signatures, confirming that molecular substitution modifies solid-state organization. Importantly, however, the mean Scherrer-derived coherent-domain-size sequence (Py-4 > Py-1 > Py-3 > Py-2) does not reproduce the field-effect mobility sequence (Py-3 > Py-4 > Py-2 > Py-1). Py-3 instead combines defined low-angle periodicity with broader short-range structural correlations, whereas Py-4 exhibits the largest individual and mean apparent coherent-domain sizes. These observations further demonstrate that crystallographic coherence length alone is not a sufficient predictor of field-effect transport and must be considered together with mesoscale connectivity, interfacial trapping, and contact/channel resistance.

These optical differences become considerably more informative when interpreted together with the SEM and AFM observations. Py-1 forms a comparatively compact and weakly structured film without pronounced long-range interconnected domains. Py-2 develops more evident nanoscale connectivity, whereas Py-3 exhibits the most pronounced fibrillar and directionally organized morphology within the series. In contrast, Py-4 forms densely aggregated nanodomains accompanied by topographical protrusions and increased morphological heterogeneity. Thus, the progression from Py-1 to Py-3 represents not merely increasing aggregation but an evolution toward a more

interconnected transport morphology, whereas the transition from Py-3 to Py-4 represents a shift toward stronger but less spatially uniform aggregation.

This distinction is directly reflected in the OFET characteristics. The field-effect mobility increases from 6.9×10^{-3} cm² V⁻¹ s⁻¹ for Py-1 to 9.3×10^{-2} cm² V⁻¹ s⁻¹ for Py-2 and reaches 5.4×10^{-1} cm² V⁻¹ s⁻¹ for Py-3. The mobility subsequently decreases to 2.25×10^{-1} cm² V⁻¹ s⁻¹ for Py-4 despite the pronounced aggregation observed for this derivative. This highlights the strong sensitivity of effective field-effect transport to substituent-dependent film organization. More importantly, the subsequent decrease in mobility for Py-4 indicates that increasing intermolecular association beyond an optimal level of structural organization does not necessarily improve macroscopic carrier transport.

A similar relationship is evident in the switching parameters. Py-3 exhibits the highest Ion/Ioff ratio (8.0×10^4), the lowest SS (1.6 V dec⁻¹), and the smallest ΔVth (1.1 V) among the representative devices. In contrast, Py-4 exhibits Ion/Ioff = 4.7×10^3, SS = 4.3 V dec⁻¹, and ΔVth = 9.4 V. Consequently, Py-4 retains relatively favorable mobility while simultaneously exhibiting substantially poorer switching stability and gate control. This behavior supports the interpretation that charge-transport efficiency and trapping behavior respond differently to film organization. Local intermolecular coupling may sustain relatively efficient hole transport in Py-4, whereas structural heterogeneity and nonuniform interfacial environments can increase the population of trapping sites that contribute to subthreshold degradation and hysteresis [5,7,17,18].

The TLM results provide an independent resistance-based assessment that is consistent with this interpretation. The contact resistance decreases from 255.53 MΩ for Py-1 to 121.23 MΩ for Py-2, then to 50.49 MΩ for Py-3, before increasing to 75.43 MΩ for Py-4. The sheet resistance follows the same sequence, decreasing from 3822 MΩ sq⁻¹ for Py-1 to 2368 MΩ sq⁻¹ for Py-2 and 1159 MΩ sq⁻¹ for Py-3, followed by an increase to 1814 MΩ sq⁻¹ for Py-4. Therefore, the superior field-effect performance of Py-3 is accompanied by simultaneous improvements in both channel and contact transport. This agreement is particularly important because it indicates that the mobility enhancement cannot be explained solely by contact-induced changes in apparent transistor performance [36,37,40].

The relationship among the independently measured parameters can therefore be summarized as a coherent transport hierarchy. Py-1 combines weak morphological connectivity with the lowest mobility and current modulation and the highest contact and sheet resistances. Py-2 represents an

intermediate regime in which improved molecular organization produces measurable enhancement in both field-effect and resistance characteristics. Py-3 establishes the optimum balance, combining interconnected fibrillar organization with the highest mobility and Ion/Ioff ratio, the lowest SS and hysteresis, and the lowest Rc and Rsh. Py-4 demonstrates the opposite side of this structural optimum: although substantial aggregation preserves relatively strong current transport, excessive morphological heterogeneity is accompanied by increased resistance, poorer subthreshold characteristics, and pronounced hysteresis.

The statistical analysis further demonstrates that this hierarchy is not restricted to selected representative devices. Across three independently characterized transistors, Py-3 retains a mean mobility of $(5.43 \pm 0.33) \times 10^{-1}$ cm² V⁻¹ s⁻¹, $I_{on}/I_{off} = (8.00 \pm 0.65) \times 10^{4}$, SS = 1.7 ± 0.1 V dec⁻¹, and ΔV_{th} = 1.2 ± 0.1 V. The relatively narrow device-to-device distributions indicate that the optimum transport characteristics associated with Py-3 are reproducible under the investigated fabrication conditions. In contrast, the consistently large hysteresis observed for Py-4 confirms that its trapping-dominated switching behavior is a reproducible characteristic at the molecular and film levels rather than an isolated device anomaly.

The positive signs of the tabulated field-effect are qualitatively consistent with the p-channel OFET response. Given the unresolved unit and geometry questions in the field-effect dataset, this observation is presented as supportive but not definitive independent verification of carrier polarity.

A comparison of representative pyrene-based OFETs reported in the literature is provided in Table 3.6. The reported performance of pyrene-derived semiconductors spans several orders of magnitude and depends strongly on molecular architecture, processing route, dielectric interface, film crystallinity, molecular packing, and device configuration. Highly ordered microribbons, single-crystalline, liquid-crystalline, π-extended, and, more recently, heteroatom- and substitution-site-engineered pyrene systems can exhibit mobilities substantially higher than those of conventional solution-processed molecular films [47–53,56]. Direct comparison of absolute mobility values must be made with caution, as differences in crystallinity, device geometry, dielectric capacitance, electrode configuration, carrier polarity, processing conditions, and mobility-extraction methodology can substantially influence the reported values [37,40].

Table 3.6. Comparison of the OFET performance of Py-1–Py-4 with representative pyrene-based organic semiconductors reported in the literature.

Channel material	Processing / morphology	Dielectric / device configuration	μ_{FE} ($cm^2 V^{-1} s^{-1}$)	Ion/Ioff	Vth (V)	SS (mV dec^{-1})	Key feature	Ref.
Py-1	Solution-processed thin film	PiBMA; TG/BC	**6.9×10^{-3}**	**1.6×10^{2}**	**−12.7**	**6500**	Compact morphology; weakest transport	This work
Py-2	Solution-processed thin film	PiBMA; TG/BC	**9.3×10^{-2}**	**2.8×10^{3}**	**−8.2**	**3800**	Improved molecular organization	This work
Py-3	Solution-processed thin film	PiBMA; TG/BC	**5.4×10^{-1}**	**8.0×10^{4}**	**−4.9**	**1600**	Interconnected fibrillar morphology; optimum overall performance	This work
Py-4	Solution-processed thin film	PiBMA; TG/BC	**2.25×10^{-1}**	**4.7×10^{3}**	**−9.6**	**4300**	Strong aggregation accompanied by increased hysteresis	This work
1-Imino nitroxide pyrene	Vapor-deposited film	OFET	**0.10**	**≈5×10^{4}**	**≈−0.6**	**≈540**	Low-voltage p-type pyrene OFET	[47]
PY-4(THB)	Single-crystalline microribbon via solution self-assembly	OTS/SiO_2/Si; BG/TC	**0.70**	**>10^{6}**	**−10**	N/R	Highly crystalline, slip-stacked microribbon transport	[48]
Pyrene end-capped terthiophene (3s)	Thin film	OTS-treated SiO_2/Si	**0.11**	N/R	N/R	N/R	Pyrene end-capped oligothiophene	[49]
P(DTDPP-alt-(2,7)PY)	Solution-processed conjugated polymer	N/R	**0.23**	**≈10^{6}**	N/R	N/R	Positional engineering of pyrene–DPP polymer; morphology-dependent transport	[50]
BOBTP	Optimized deposited thin film; liquid-crystalline semiconductor	SAM-modified gate dielectric	**2.10**	**7.6×10^{6}**	N/R	N/R	Optimized molecular packing and dielectric-interface engineering	[51]

Channel material	Processing / morphology	Dielectric / device configuration	μ_{FE} (cm^2 V^{-1} s^{-1})	Ion/Ioff	Vth (V)	SS (mV dec^{-1})	Key feature	Ref.
BPy2T	Single-crystal OFET	N/R	**3.30**	N/R	N/R	N/R	2-positional pyrene end-capped oligothiophene; single-crystal transport	[52]
Pyrene end-capped triarylamine	Thin film	BG/TC	**2.5**	**10^7**	**−7**	N/R	D–π–D′ architecture; molecular ordering and favorable hole injection	[53]
1,6-5FPyNN	Polycrystalline thin film; interconnected elongated grains	n-type OFET	**1.64 ± 0.29**	**>10^5**	N/R	N/R	Heteroatom doping and substitution-site engineering; 2D brickwork packing	[56]

N/R = not reported or not sufficiently verifiable from the primary-source information available. TG/BC = top-gate/bottom-contact; BG/TC = bottom-gate/top-contact.

Within this context, the significance of the present Py-1–Py-4 series does not arise from achieving a record absolute mobility. Instead, its principal contribution lies in demonstrating, within a common molecular platform and identical OFET architecture, how systematic substituent modification is associated with coordinated changes in optical response, nanoscale morphology, switching hysteresis, contact resistance, channel resistance, and field-effect transport. The best-performing Py-3 device achieves μ_{FE} = 5.4 × 10 -1 cm^2 V^{-1} s^{-1} and I_{on}/I_{off} = 8.0 × 10^4 under solution-processed thin-film conditions. Although substantially higher mobilities have been reported for highly crystalline, extensively π-extended, or recently engineered pyrene semiconductors [47–53,56], the internally controlled Py-1–Py-4 comparison enables evaluation of the influence of molecular substitution and the resulting film organization across multiple complementary electrical metrics under otherwise identical fabrication conditions.

The comparison also emphasizes the role of processing and structural dimensionality. Literature systems employing single crystals or highly ordered self-assembled structures can minimize grain boundaries and energetic disorder, thereby providing substantially higher mobilities [48,51,52]. In contrast, the present devices are based on solution-processed molecular thin films, in which

intermolecular connectivity and interfacial quality are particularly important. The substantial enhancement from Py-1 to Py-3 under otherwise identical fabrication conditions therefore supports the conclusion that rational molecular modification can improve charge transport even without resorting to single-crystal growth or highly specialized device processing.

These observations are consistent with the broader understanding of organic semiconductor transport, in which molecular design, mesoscale organization, dielectric-interface properties, and electrode/semiconductor interactions collectively influence the effective field-effect response [3,5,6,12,40]. Related trends have also been observed in our recent transistor studies employing chemically and structurally modified semiconductor environments. In diazonium-functionalized P3HT: RGO OFETs, controlled chemical modification of the carbon component produced systematic changes in field-effect transport and switching characteristics [54]. Similarly, carbon hybridization of CVD-grown monolayer MoS_2 led to systematic changes in transistor transport and resistance characteristics [55]. Although these systems differ materially from the present pyrene semiconductors, they provide complementary evidence that controlled modification of the semiconductor environment can be reflected simultaneously in transport, interfacial response, and device switching behavior.

Overall, the combined results establish a multiscale structure–energetics–morphology–interface–transport relationship in which molecular substitution simultaneously modifies intrinsic hole-formation energetics, solid-state film organization, and the resulting channel- and interface-related transport characteristics. The best overall response observed for Py-3 coincides with a favorable combination of interconnected fibrillar morphology, reduced contact and sheet resistance, low hysteresis, and enhanced field-effect transport. In contrast, the behavior of Py-4 demonstrates that stronger but heterogeneous aggregation can coexist with increased resistance and trapping despite relatively favorable carrier transport. This experimentally supported distinction between beneficial mesoscale connectivity and excessive heterogeneous aggregation represents the central design insight emerging from the present study and highlights substituent engineering as a practical strategy for tuning solution-processed pyrene-based organic semiconductors.

4. Conclusions

A systematic molecular-to-device investigation was conducted to determine how substituent engineering affects charge transport in a series of pyrene-based organic semiconductors (Py-1–Py-4). By integrating molecular electronic-structure calculations with optical response, X-ray diffraction, thin-film morphology, field-effect, OFET characteristics, channel-length-dependent resistance, and device statistics within a common framework, the study establishes a multiscale structure–energetics–morphology–interface–transport relationship across an internally consistent molecular series.

Pronounced substituent-dependent differences were observed in optical response and solid-state film organization. SEM and AFM revealed an evolution from the comparatively compact morphology of Py-1 toward increasingly interconnected domains, culminating in the pronounced fibrillar organization of Py-3. Py-4, in contrast, exhibited stronger but spatially heterogeneous aggregation characterized by densely clustered nanodomains and pronounced topographical features. These morphological differences were accompanied by systematic changes in the electrical characteristics of the corresponding OFETs. The molecular-level calculations further showed that Py-3 combines the lowest adiabatic ionization potential (6.447 eV) with a relatively low internal hole reorganization energy (0.186 eV). However, Py-2 exhibits the lowest λh (0.178 eV), while Py-3 and Py-4 possess nearly identical λh values despite their markedly different transistor characteristics. These results demonstrate that favorable intrinsic hole-transport energetics constitute an important molecular contribution but do not independently determine the device-level transport hierarchy.

Among the investigated derivatives, Py-3 exhibited the best overall transistor performance, with a field-effect mobility of 5.4×10^{-1} cm^2 V^{-1} s^{-1}, an Ion/Ioff ratio of 8.0×10^4, a subthreshold swing of 1.6 V dec^{-1}, and threshold-voltage hysteresis of only 1.1 V. In contrast, Py-4 retained a comparatively high mobility of 2.25×10^{-1} cm^2 V^{-1} s^{-1} but exhibited substantially increased hysteresis (9.4 V) and poorer subthreshold behavior. TLM analysis provided complementary resistance-based evidence, with Py-3 exhibiting the lowest contact resistance (50.49 MΩ) and sheet resistance (1159 MΩ sq^{-1}), while statistical measurements across independently fabricated devices preserved the same performance hierarchy. Together, these results indicate that the superior field-effect response of Py-3 is associated with simultaneous improvements in channel-related transport, contact characteristics, gate control, and device reproducibility rather than an isolated increase in drain current or apparent mobility.

Taken together, the computational, optical, diffraction, morphological, electrical, OFET, TLM, and statistical results demonstrate that efficient field-effect transport in this molecular series emerges from the interplay between favorable intrinsic molecular energetics and an interconnected, comparatively uniform solid-state transport network. The present study therefore moves beyond mobility-oriented screening and provides an experimentally supported framework for relating molecular substitution to nanoscale film organization, interfacial response, and macroscopic field-effect transport in solution-processed pyrene semiconductors. The inferred association between fibrillar connectivity and reduced trapping is supported by correlated morphological and electrical observations, rather than direct spatially resolved measurements of individual trapping sites.

Supporting Information

The accompanying Supporting Information includes detailed experimental characterization data for Py-1–Py-4, ^{1}H and ^{13}C NMR spectra, ESI-QTOF mass spectra, provisionally vacuum-referenced electrochemical energy-level estimates and measured redox onset potentials, optimized neutral and radical-cation geometries, calculated HOMO/LUMO distributions, four-point energy components used to determine internal hole reorganization energies and adiabatic ionization potentials, and spin-state diagnostics for radical-cation calculations.

References

[1] S. R. Forrest, The path to ubiquitous and low-cost organic electronic appliances on plastic, Nature 2004, 428, 911–918.

[2] A. Facchetti, π-Conjugated Polymers for Organic Electronics and Photovoltaic Cell Applications, Chem. Mater. 2011, 23, 733–758.

[3] J. E. Anthony, Functionalized Acenes and Heteroacenes for Organic Electronics, Chem. Rev. 2006, 106, 5028–5048.

[4] C. D. Dimitrakopoulos, P. R. L. Malenfant, Organic Thin Film Transistors for Large Area Electronics, Adv. Mater. 2002, 14, 99–117.

[5] H. Sirringhaus, 25th Anniversary Article: Organic Field-Effect Transistors: The Path Beyond Amorphous Silicon, Adv. Mater. 2014, 26, 1319–1335.

[6] R. Noriega, J. Rivnay, K. Vandewal, F. P. V. Koch, N. Stingelin, P. Smith, M. F. Toney, A. Salleo, A general relationship between disorder, aggregation and charge transport in conjugated polymers, Nat. Mater. 2013, 12, 1038–1044.

[7] A. Salleo, Charge transport in polymeric transistors, Mater. Today 2007, 10, 38–45.

[8] J. Roncali, Molecular Engineering of the Band Gap of π-Conjugated Systems: Facing Technological Applications, Macromol. Rapid Commun. 2007, 28, 1761–1775.

[9] T. M. Figueira-Duarte, K. Müllen, Pyrene-Based Materials for Organic Electronics, Chem. Rev. 2011, 111, 7260–7314.

[10] J. B. Birks, Excimers, Rep. Prog. Phys. 1975, 38, 903–974.

[11] F. Würthner, Perylene bisimide dyes as versatile building blocks for functional supramolecular architectures, Chem. Commun. 2004, 1564–1579.

[12] V. Coropceanu, J. Cornil, D. A. da Silva Filho, Y. Olivier, R. Silbey, J.-L. Brédas, Charge transport in organic semiconductors, Chem. Rev. 2007, 107, 926–952.

[13] A. Troisi, Prediction of the Absolute Charge Mobility of Molecular Semiconductors: the Case of Rubrene, Adv. Mater. 2007, 19, 2000–2004.

[14] P. M. Beaujuge, J. R. Reynolds, Color Control in π-Conjugated Organic Polymers for Use in Electrochromic Devices, Chem. Rev. 2010, 110, 268–320.

[15] Y. Lin, Y. Li, X. Zhan, Small molecule semiconductors for high-efficiency organic photovoltaics, Chem. Soc. Rev. 2012, 41, 4245–4272.

[16] L. Duan, L. Hou, T. Lee, J. Qiao, D. Zhang, G. Dong, L. Wang, Y. Qiu, Solution processable small molecules for organic light-emitting diodes, J. Mater. Chem. 2010, 20, 6392–6407.

[17] J. Veres, S. D. Ogier, S. W. Leeming, D. C. Cupertino, S. Mohialdin Khaffaf, Low-k Insulators as the Choice of Dielectrics in Organic Field-Effect Transistors, Adv. Funct. Mater. 2003, 13, 199–204.

[18] W. L. Kalb, B. Batlogg, Calculating the trap density of states in organic field-effect transistors from experiment: A comparison of different methods, Phys. Rev. B 2010, 81, 035327.

[19] J. Mei, D. H. Kim, A. L. Ayzner, M. F. Toney, Z. Bao, Siloxane-Terminated Solubilizing Side Chains: Bringing Conjugated Polymer Backbones Closer and Boosting Hole Mobilities in Thin-Film Transistors, J. Am. Chem. Soc. 2011, 133, 20130–20133.

[20] K. Takimiya, H. Ebata, K. Sakamoto, T. Izawa, T. Otsubo, Y. Kunugi, 2,7-Diphenyl[1]benzothieno[3,2-b]benzothiophene, A New Organic Semiconductor for Air-Stable Organic Field-Effect Transistors with Mobilities up to 2.0 $cm^2 V^{-1} s^{-1}$, J. Am. Chem. Soc. 2006, 128, 12604–12605.

[21] J.-L. Brédas, J.-P. Calbert, D. A. da Silva Filho, J. Cornil, Organic semiconductors: A theoretical characterization of the basic parameters governing charge transport, Proc. Natl. Acad. Sci. U.S.A. 2002, 99, 5804–5809.

[22] Y. D. Park, H. S. Lee, Y. J. Choi, D. Kwak, J. H. Cho, S. Lee, K. Cho, Solubility-Induced Ordered Polythiophene Precursors for High-Performance Organic Thin-Film Transistors, Adv. Funct. Mater. 2009, 19, 1200–1206.

[23] J. Gierschner, S. Y. Park, Luminescent Distyrylbenzenes: Tailoring Molecular Structure and Crystalline Morphology, J. Mater. Chem. C 2013, 1, 5818–5832.

[24] C. B. Nielsen, S. Holliday, H.-Y. Chen, S. J. Cryer, I. McCulloch, Non-Fullerene Electron Acceptors for Use in Organic Solar Cells, Acc. Chem. Res. 2015, 48, 2803–2812.

[25] T. Someya, Y. Kato, T. Sekitani, S. Iba, Y. Noguchi, Y. Murase, H. Kawaguchi, T. Sakurai, Conformable, flexible, large-area networks of pressure and thermal sensors with organic transistor active matrixes, Proc. Natl. Acad. Sci. U.S.A. 2005, 102, 12321–12325.

[26] C. Li, H. Wonneberger, Perylene imides for organic photovoltaics: yesterday, today, and tomorrow, Adv. Mater. 2012, 24, 613–636.

[27] G. Socrates, Infrared and Raman Characteristic Group Frequencies: Tables and Charts, 3rd ed., Wiley, Chichester, UK 2004.

[28] J. Coates, in Encyclopedia of Analytical Chemistry, Wiley, Chichester, UK 2000.

[29] R. M. Silverstein, F. X. Webster, D. J. Kiemle, Spectrometric Identification of Organic Compounds, 7th ed., Wiley, Hoboken, NJ, USA 2005.

[30] N. B. Colthup, L. H. Daly, S. E. Wiberley, Introduction to Infrared and Raman Spectroscopy, 3rd ed., Academic Press, Boston, MA, USA 1990.

[31] B. Valeur, M. N. Berberan-Santos, Molecular Fluorescence: Principles and Applications, 2nd ed., Wiley-VCH, Weinheim, Germany 2012.

[32] F. Würthner, T. E. Kaiser, C. R. Saha-Möller, J-Aggregates: From Serendipitous Discovery to Supramolecular Engineering of Functional Dye Materials, Angew. Chem. Int. Ed. 2011, 50, 3376–3410.

[33] X. Feng, X. Wang, C. Redshaw, B. Z. Tang, Aggregation behaviour of pyrene-based luminescent materials, from molecular design and optical properties to application, Chem. Soc. Rev. 2023, 52, 6715–6753.

[34] H.-I. Un, J.-Y. Wang, J. Pei, Recent Efforts in Understanding and Improving the Nonideal Behaviors of Organic Field-Effect Transistors, Adv. Sci. 2019, 6, 1900375.

[35] F. Kuang, F. Wang, D. Duan, Y. Ma, X. Sun, S. Satapathi, A. Ng, H. Lin, Z. Li, Y. Zhong, H. Hu, Organic field-effect transistors: Materials design, device physics, and contact engineering for high-performance flexible electronics, Inf. Funct. Mater. 2025, 2, 267–305.

[36] M. Waldrip, O. D. Jurchescu, D. J. Gundlach, E. G. Bittle, Contact Resistance in Organic Field-Effect Transistors: Conquering the Barrier, Adv. Funct. Mater. 2020, 30, 1904576.

[37] C. Liu, Y. Xu, Y.-Y. Noh, Contact engineering in organic field-effect transistors, Mater. Today 2015, 18, 79–96.

[38] S. Donnhäuser, A. Pacheco-Sanchez, K. Haase, S. C. B. Mannsfeld, M. Claus, S. Blawid, Impact of injection limitations on the contact resistance and the carrier mobility of organic field effect transistors, Org. Electron. 2021, 99, 106343.

[39] G. Horowitz, R. Hajlaoui, H. Bouchriha, R. Bourguiga, M. Hajlaoui, The Concept of "Threshold Voltage" in Organic Field-Effect Transistors, Adv. Mater. 1998, 10, 923–927.

[40] D. Natali, M. Caironi, Charge Injection in Solution-Processed Organic Field-Effect Transistors: Physics, Models and Characterization Methods, Adv. Mater. 2012, 24, 1357–1387.

[41] D. K. Schroder, Semiconductor Material and Device Characterization, 3rd ed., Wiley, Hoboken, NJ, USA 2006.

[42] T. J. Richards, H. Sirringhaus, Analysis of the contact resistance in staggered, top-gate organic field-effect transistors, J. Appl. Phys. 2007, 102, 094510.

[43] V. Verma, D. Dahal, R. K. R. Krishnan, B. Lüssem, T.-H. Tsai, Accurate and reproducible mobility estimation enables high-throughput analysis of organic field-effect transistors, Comput. Mater. Sci. 2022, 214, 111689.

[44] S. Lai, K. Kumpf, P. C. Ricci, P. Fruhmann, J. Bintinger, A. Bonfiglio, P. Cosseddu, Isotropic contact patterning to improve reproducibility in organic thin-film transistors, Org. Electron. 2023, 122, 106887.

[45] R. Ahmed, M. Sams, C. P. Simbrunner, M. Ullah, K. Rehman, G. Schwabegger, H. Sitter, T. Ostermann, Reproducibility and stability of C60 based organic field effect transistor, Synth. Met. 2012, 161, 2562–2565.

[46] R. Gao, P. Yuan, X. Zhang, S. Sang, X.-C. Hang, H. Nan, C. Liu, C. Zhang, X. Gao, F. Chen, X. Guo, Z.-K. Chen, An Asymmetric Molecular Design Strategy for Organic Field-Effect Transistors with High Consistency of Performance, ACS Appl. Electron. Mater. 2019, 1, 1233–1242.

[47] Y. Wang, H. Wang, Y. Liu, C.-A. Di, Y. Sun, W. Wu, G. Yu, D. Zhang, D. Zhu, 1-Imino Nitroxide Pyrene for High Performance Organic Field-Effect Transistors with Low Operating Voltage, J. Am. Chem. Soc. 2006, 128, 13058–13059.

[48] Y. S. Kim, S. Y. Bae, K. H. Kim, T. W. Lee, J. A. Hur, M. H. Hoang, M. J. Cho, S.-J. Kim, Y. Kim, M. Kim, K. Lee, S. J. Lee, D. H. Choi, Highly sensitive phototransistor with crystalline microribbons from new π-extended pyrene derivative via solution-phase self-assembly, Chem. Commun. 2011, 47, 8907–8909.

[49] J. Kwon, J.-P. Hong, S. Noh, T.-M. Kim, J.-J. Kim, C. Lee, S. Lee, J.-I. Hong, Pyrene end-capped oligothiophene derivatives for organic thin-film transistors and organic solar cells, New J. Chem. 2012, 36, 1813–1818.

[50] D. S. Yang, K. H. Kim, M. Cho, J. I. Jin, D. H. Choi, Donor–acceptor alternating π-conjugated polymers containing Di(thiophen-2-yl)pyrene and 2,5-Bis(2-octyldodecyl)pyrrolo[3,4-c]pyrrole-1,4(2H,5H)-dione for organic thin-film transistors, J. Polym. Sci., Part A: Polym. Chem. 2013, 51, 1457–1467.

[51] H. Cho, S. Lee, N. S. Cho, G. E. Jabbour, J. Kwak, D.-H. Hwang, C. Lee, High-mobility pyrene-based semiconductor for organic thin-film transistors, ACS Appl. Mater. Interfaces 2013, 5, 3855–3860.

[52] K. Oniwa, H. Kikuchi, H. Shimotani, S. Ikeda, N. Asao, Y. Yamamoto, K. Tanigaki, T. Jin, 2-Positional pyrene end-capped oligothiophenes for high performance organic field effect transistors, Chem. Commun. 2016, 52, 4800–4803.

[53] P. Devibala, B. Balambiga, P. M. Imran, N. S. P. Bhuvanesh, S. Nagarajan, Synthesis of Anthracene and Pyrene End-Capped Triarylamines for p-Channel High-Performance OFETs, Eur. J. Org. Chem. 2022, 2022, e202200825.

[54] Z. Kudaş, H. F. Budak, D. Ekinci, B. Güzeldir, Interface-controlled charge transport in P3HT:RGO hybrid OFETs: role of diazonium functionalization and gate dielectric thickness scaling, Appl. Surf. Sci. 2026, 745, 167521.

[55] E. Daş, A. E. Kasapoğlu, M. A. Takar, M. Koç, M. Sağlam, B. Güzeldir, Enhanced electrical transport in CVD-grown monolayer MoS_2 thin-film transistors via carbon hybridization, Diamond Relat. Mater. 2026, 169, 114055.

[56] H. Li, Y. Zhang, Z. Miao, Z. Peng, H. Tian, L. Wang, Synergistic modulation by heteroatom doping and substitution site isomerism: Development of high-performance pyrene-based n-type small-molecule semiconductors, Org. Electron. 2026, 155, 107443.

[57] Q. Sun, T. C. Berkelbach, N. S. Blunt, G. H. Booth, S. Guo, Z. Li, J. Liu, J. D. McClain, E. R. Sayfutyarova, S. Sharma, S. Wouters, G. K.-L. Chan, PySCF: the Python-based simulations of chemistry framework, WIREs Comput. Mol. Sci. 2018, 8, e1340.

Supplementary Files

This is a list of supplementary files associated with this preprint. Click to download.

- SupportingInformation.docx